Dear Editor,

Thank you for handling our manuscript, "A new High-Resolution daily Mean South China Sea Ocean Reanalysis dataset: SCSORA" (essd-2026-440), and for coordinating the review process. We also sincerely thank the reviewers for their constructive comments, which have helped us substantially improve the manuscript. We have carefully addressed each comment and revised the manuscript accordingly.

This document contains our point-by-point responses to all reviewer comments, together with the marked-up manuscript showing all changes. Author responses are shown in blue, and all changes to the manuscript are indicated by track changes in the marked-up manuscript. The line numbers cited in our responses refer to the marked-up manuscript (Revised_Manuscript_with_Track_Changes.pdf).

We hope that the revised manuscript now meets the standards for publication in ESSD. Our point-by-point responses to the reviewers are provided below.

Sincerely,

Xueming Zhu

Response to Reviewer #1:

We thank the reviewer for the constructive comments, which have helped us significantly improve the manuscript. We have carefully addressed each comment and revised the manuscript accordingly. The main revisions include clarifying the open boundary conditions and model configuration, explaining how the EnOI scheme handles sparse Argo data with additional glider-based validation, updating the SLA product URL, adding OISST dataset to the SST and MHW analyses, discussing the seasonal and interannual variations of SST and SLA RMSE, confirming the consistency of the MLD estimation method, and providing a detail discussion of the high eddy counts in SCSORA during 2022–2024. Detailed point-by-point responses are given below, together with the corresponding changes in the revised manuscript.

1. L100-102: What global reanalysis data is used for open boundary conditions?

Response: The open boundary conditions are derived from SODA 3.15.2 data by spatially interpolating, as clarified in the revised manuscript (Lines 143-144). Meanwhile, we have also expanded Section 2.1 (SCSOFSv2 Model Description, lines 130-175) to describe the model configuration in more detail, including the model domain, grid, vertical coordinate, time steps, initial and boundary conditions, atmospheric forcing, advection and mixing schemes, and the EnOI data assimilation system.

Changes in the manuscript:

(1) We have clarified the open boundary data source in lines 143–144, which now read:

" The open boundary values of temperature, salinity, velocity, and SSH are obtained by spatial interpolation of SODA 3.15.2 dataset."

(2) We have expanded Section 2.1 (Lines 130-175) to provide a more complete description of the SCSOFSv2 configuration. The revised text is provided below:

" The SCSORA dataset released in this study is generated by SCSOFSv2. SCSOFSv2 is built on the Regional Ocean Modeling System (ROMS). Its domain covers the SCS and its adjacent waters (99–144° E, 4.5° S–28.3° N). The horizontal grid is curvilinear orthogonal with a resolution of 1/30° in the SCS. The vertical coordinate uses 50 terrain-following σ layers with an improved double stretching function (Shchepetkin and McWilliams, 2005), ensuring sufficient vertical resolution within the upper 300 m to resolve the mixed layer and thermocline structure; the thinnest near-surface layer is approximately 0.09 m. The barotropic and baroclinic time steps are 5 s and 150 s, respectively.

The initial temperature and salinity fields are taken from the January monthly mean of the Generalized Digital Environmental Model version 3.0 (GDEMv3; Carnes, 2009) global climatology. The surface atmospheric forcing is provided by the ECMWF ERA5 reanalysis

(Hersbach et al., 2020) at a horizontal resolution of 0.25°. The forcing variables include 10 m wind speed, mean sea level pressure, 2 m air temperature, 2 m relative humidity, downward longwave radiation flux, precipitation rate, and shortwave radiation flux. All four lateral boundaries are opened. At the open boundaries, the Chapman (1985) boundary condition is applied to the free surface, and the Flather (1976) radiation condition is applied to the depth-averaged (barotropic) velocity. The 3D velocity components, temperature, and salinity are treated using radiation–nudging boundary conditions following Marchesiello et al. (2001). The open boundary values of temperature, salinity, velocity, and SSH are obtained by spatial interpolation of SODA 3.15.2 dataset. For tracer advection, SCSOFSv2 uses the fourth-order Akima scheme (Shchepetkin and McWilliams, 2005) in both the horizontal and vertical directions. For momentum advection, a third-order upstream scheme is used in the horizontal direction and a fourth-order centred scheme in the vertical direction. Vertical turbulent mixing for both momentum and tracers is parameterised using the Mellor–Yamada level 2.5 closure scheme (Mellor and Yamada, 1982).

The system employs an EnOI data assimilation scheme (Evensen, 2003; Oke et al., 2008), assimilating three categories of observations: satellite-derived SST, along-track satellite SLA, and in-situ temperature–salinity profiles. The along-track SLA data are filtered with a Lanczos low-pass filter (cut-off wavelength 65 km, 20-day period) and are not subsampled. Observation errors are set to 3 cm for SLA (Taburet et al., 2018) and are depth-dependent for Argo profiles following Xie and Zhu (2010). To account for asynchronous observations within the assimilation time window, the First Guess at Appropriate Time (FGAT) approach is adopted to reduce assimilation biases arising from observation timing errors. The background error covariance is constructed from an ensemble of model anomalies. A Hanning low-pass filter is applied to the running mean to retain intraseasonal variability, and the anomalies are computed by subtracting the 20-day running mean from the 10-year (1991-2000) free-run daily averaged results. The assimilation cycle is 7 days. Within each cycle, all SLA and Argo observations within the 7-day time window, and SST data 1-day before the analysis date are used. It should be noted that the number of Argo profiles in the SCS was very limited in the early 2000s and remains relatively sparse in the shallow southern SCS. To mitigate this data sparsity, the assimilation system also relies on satellite SST and along-track SLA observations, which provide better spatiotemporal coverage. In addition, the ensemble-based background error covariance allows an Argo observation to influence nearby model variables within a localization radius of 150 km."

2. L125-126: The number of Argo floats should be small in the SCS in the early 2000s. Also, the number of Argo floats should be limited in the southern SCS because the depth

is shallow in the region. Please comment more about how the assimilation using Argo data works in the SCS.

Response: We fully agree that the number of Argo floats in the SCS was indeed very limited in the early 2000s. Below we describe the actual distribution of SCS Argo data and explain how the SCSOFSv2 assimilation system handles this data sparsity.

The global Argo array was gradually deployed in the early 2000s and only reached its target of approximately 3,000 floats around 2007 (Roemmich et al., 2009). As a marginal sea of the northwestern Pacific Ocean, the SCS began to see a gradual increase in available Argo profiles after 2006. Despite this sparse coverage, the SCSOFSv2 assimilation system still exploits the available Argo profiles through the following mechanisms:

(1) Spatially correlated ensemble background error covariance. The EnOI scheme constructs the background error covariance from model anomalies of a 10-year (1991–2000) free run. This ensemble-based covariance inherently contains spatial correlations, so an Argo observation at one location can influence nearby model variables through the covariance structure. With a localization radius of 150 km, the influence of each Argo profile is spatially limited but still allows information to propagate to neighboring regions.

(2) Complementary multi-source observations. Argo profiles are assimilated together with satellite SST and along-track SLA. In regions and periods where Argo data are sparse, satellite observations with better spatiotemporal coverage still constrain the sea surface and column-integrated ocean state.

(3) Temporal extension of observation impact through FGAT and IAU. The FGAT approach computes observation innovations within 56 three-hour slots, reducing the maximum time mismatch to 1.5 hours. IAU applies the analysis increment as a forcing term that is gradually introduced over the 7-day assimilation cycle. This means that even if Argo observations are available only on certain days, their impact is spread over the entire cycle rather than applied instantaneously, which is particularly beneficial for irregularly distributed observations (Zhu et al., 2022).

(4) Physically consistent model background. In the absence of Argo data, the model background driven by ERA5 atmospheric forcing and constrained by SODA open boundary conditions still provides a physically consistent estimate. Argo assimilation then provides corrections where and when data are available.

To evaluate the effect of assimilation in the southern SCS, we compared SCSORA and a free run without assimilation against independent glider observations from 2019. As shown in Figure R1, SCSORA reproduces the subsurface thermohaline structure substantially better than the free run, indicating that assimilation effectively improves subsurface state estimation even

in this region. In future improvements to the assimilation system, we will further assimilate additional observation types, such as gliders, subsurface moorings, and drifters, to strengthen the constraint on subsurface structure in the shallow-water region of the southern SCS.

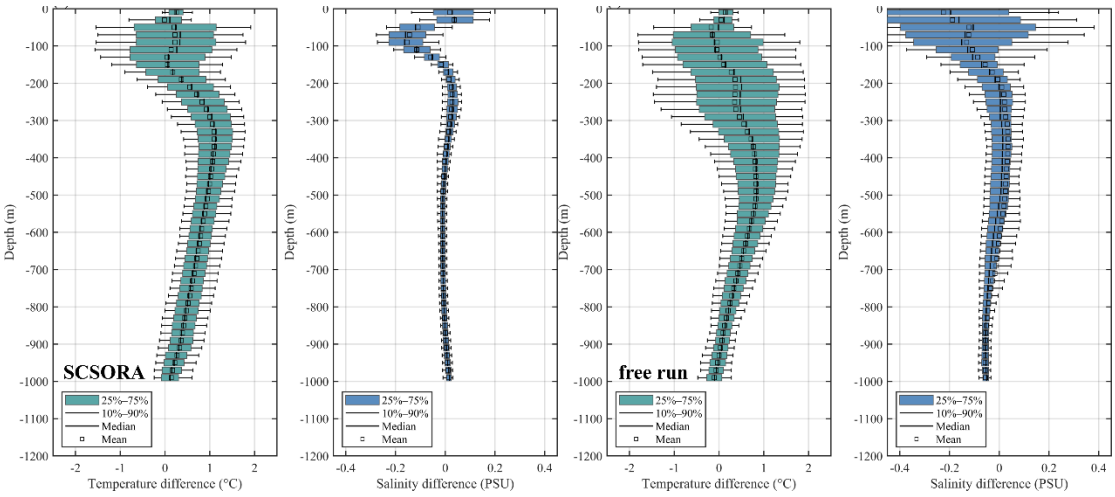


Figure R1. Vertical profiles of temperature and salinity differences for SCSORA and the free run.

Changes in the manuscript:

(1) We have added a description of the EnOI assimilation scheme and the assimilated observation types (Lines 149–151). The added text reads:

"The system employs an EnOI data assimilation scheme (Evensen, 2003; Oke et al., 2008), assimilating three categories of observations: satellite-derived SST, along-track satellite SLA, and in-situ temperature–salinity profiles. The along-track SLA data are filtered with a Lanczos low-pass filter (cut-off wavelength 65 km, 20-day period) and are not subsampled."

(2) We have added a brief description of the Argo data sparsity in the SCS and the mechanisms by which the assimilation system mitigates this sparsity in Section 2.1 (Lines 158–175). The added text reads:

" It should be noted that the number of Argo profiles in the SCS was very limited in the early 2000s and remains relatively sparse in the shallow southern SCS. To mitigate this data sparsity, the assimilation system also relies on satellite SST and along-track SLA observations, which provide better spatiotemporal coverage. In addition, the ensemble-based background error covariance allows an Argo observation to influence nearby model variables within a localization radius of 150 km."

3. L155: Please check the URL for the SLA product.

Response: We thank the reviewer for pointing this out. We have checked and updated the URL for the SLA product (Line 251 in the revised manuscript). The data are available at

https://doi.org/10.48670/moi-00148.

Changes in the manuscript:

We have updated the URL for the SLA product in line 251 of the revised manuscript. The revised text now reads:

" The data are available at https://doi.org/10.48670/moi-00148."

4. Sec. 3.1: Could you plot or check the SST anomaly of OISST (Fig. 2top)? Do the time series mostly overlap SCSORA due to the assimilation? There are annual variations in the SST RMSE: large in winter and small in summer. Is this why spatial variations are larger in winter than summer?

Response: We thank the reviewer for the valuable comments. We address each point below.

(1) In the revised manuscript, we have added the OISST SST anomaly time series to Figure 2 (Line 338). The time series of the three datasets show broadly consistent variation trends.

(2) SCSORA assimilates OISST data. In the validation, SCSORA is compared separately with OISST and OSTIA, and OSTIA is not involved in the assimilation, so it serves as an independent validation dataset. The results show a mean RMSE of 0.340°C between SCSORA and OISST, and 0.357°C between SCSORA and OSTIA. Both values are low and comparable in magnitude, indicating that SCSORA agrees well with both satellite SST products. Since OSTIA is not assimilated, the close agreement between SCSORA and OSTIA provides an independent check of the SST field.

(3) The SST RMSE exhibits a clear seasonal cycle, and the spatial patterns of RMSE are broadly consistent between the two comparisons (SCSORA vs OISST and SCSORA vs OSTIA; Figure 3, line 381 in the revised manuscript). In winter, the RMSE increases markedly in the Taiwan Strait, forming a prominent high-error band, which corresponds to the region of strong northeasterly monsoon forcing, cold coastal water transport, and pronounced SST fronts (Kuo et al., 2018). In summer, the central SCS maintains low RMSE, while a localized high-error band appears along the Vietnam coast, which may be related to southwesterly monsoon-driven coastal upwelling and offshore cold-water expansion (Xie et al., 2003). Therefore, the spatial RMSE is generally larger in winter than in summer, with a broader high-error region. This seasonal difference may be related to the seasonal intensification of monsoon-driven processes and the increased sensitivity of the model to wind forcing, vertical mixing, horizontal advection, and COARE3.0 bulk algorithm.

Changes in the manuscript:

(1) We have added the OISST SST anomaly time series to Figure 2 (Line 338). The revised figure caption now reads:

"

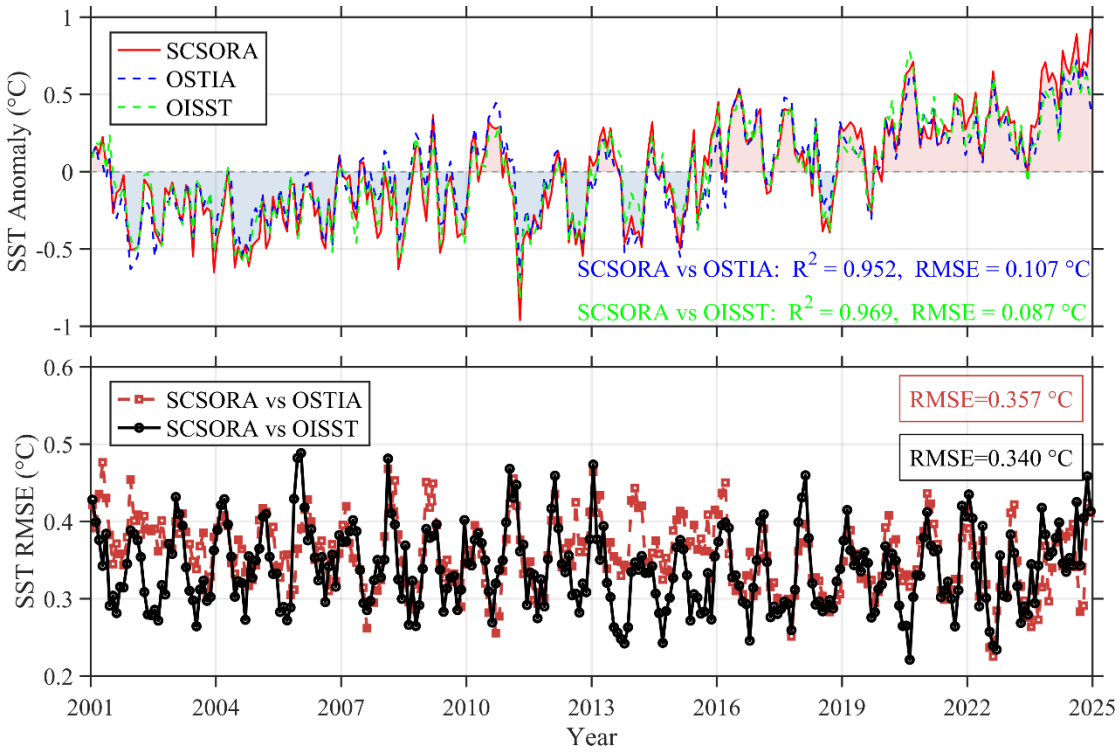


Figure 2. Time series of SST anomalies and RMSE relative to the 2001–2024 SST climatology. Comparisons are shown among SCSORA, OSTIA, and OISST. SST anomalies are computed as daily departures from the 2001–2024 climatological SST. "

(2) We have added the seasonal spatial distributions of SST RMSE between SCSORA and OISST (top row) and between SCSORA and OSTIA (bottom row) as Figure 3 (Line 381). The revised figure caption now reads:

"

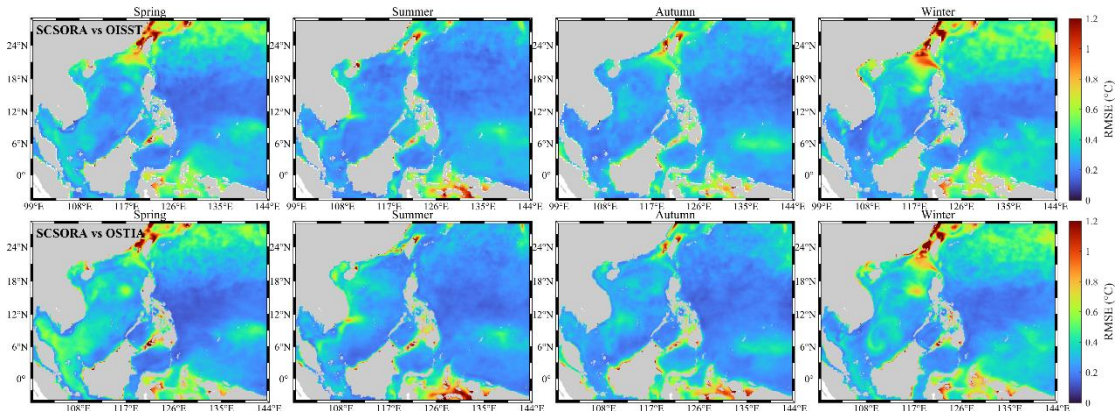


Figure 3. Seasonal spatial distributions of SST RMSE between SCSORA and OISST (top row) and between SCSORA and OSTIA (bottom row) for spring, summer, autumn, and winter (from left to right). "

(3) We have added the corresponding discussion of the seasonal RMSE patterns in Section 3.1 (Lines 354–380). The added text reads:

"The RMSE of SST between SCSORA and both OISST and OSTIA exhibits pronounced regional disparities and seasonal evolution (Figure 3). Overall, the RMSE in the central open waters of the SCS is generally below 0.5°C, whereas larger errors are predominantly distributed in the Taiwan Strait, the northern SCS continental shelf, and certain coastal regions, with localized values exceeding 0.8°C. Such spatial discrepancies may be associated with complex ocean dynamical processes in nearshore and shelf seas, such as monsoon-driven coastal circulations, tidal mixing, and local upwelling.

In terms of seasonal variability, the RMSE increases markedly during winter in the northern SCS and adjacent to the Taiwan Strait, forming a relatively prominent high-error region. Previous studies have demonstrated that the northeasterly monsoon can drive the southward transport of cold coastal water and generate a distinct SST front in the Taiwan Strait; concurrently, intensified wintertime sea surface cooling in the northern SCS further enhances the regional temperature gradient (Kuo et al., 2018). Therefore, the relatively large RMSE in these regions may be attributed to model biases in simulating monsoon-driven sea surface heat fluxes, coastal water mass transport, and the positioning of temperature fronts. As the northeasterly monsoon gradually weakens, the high-error extent in the northern SCS diminishes accordingly. During summer, the central open waters of the SCS maintain relatively low RMSE, yet a localized high-value band emerges along the Vietnam coast. Xie et al. (2003) noted that the southwesterly monsoon can drive coastal upwelling off Vietnam and promote the offshore expansion of cold water through local wind stress curl and anticyclonic circulation. These processes may intensify the local SST spatial gradient, rendering the simulated results in this region more sensitive to the accuracy of wind fields, vertical mixing, and horizontal advection. Nevertheless, SCSORA is capable of reproducing SST over most of the SCS reasonably well across all seasons, particularly exhibiting low RMSE in open waters, which indicates its favorable capability for SST reconstruction."

5. Sec. 3.2. If possible, please comment on why the SLA RMSE is relatively large in 2017-2022 (Fig. 3bottom).

Response: We further examined the temporal variations of SLA and its RMSE over 2001–2024. Figure 4 (Line 398 in the revised manuscript) shows that AVISO SLA exhibits pronounced increases around 2017 and 2021, and SCSORA reproduces these increases reasonably well, although the amplitude is generally weaker, leading to relatively larger SLA RMSE during these periods. Such increases have been reported to be associated with multiple factors, including the long-term sea level rise trend, La Niña, the PDO transition from a warm to a cool phase, typhoon-induced storm surges, and wind stress and Ekman transport during the monsoon transition (Wang et al., 2026). In SCSOFSv2, the assimilation of along-track SLA

involves a Lanczos low-pass filter, which removes part of the signal and weakens the model's ability to reproduce the full amplitude of the SLA increase.

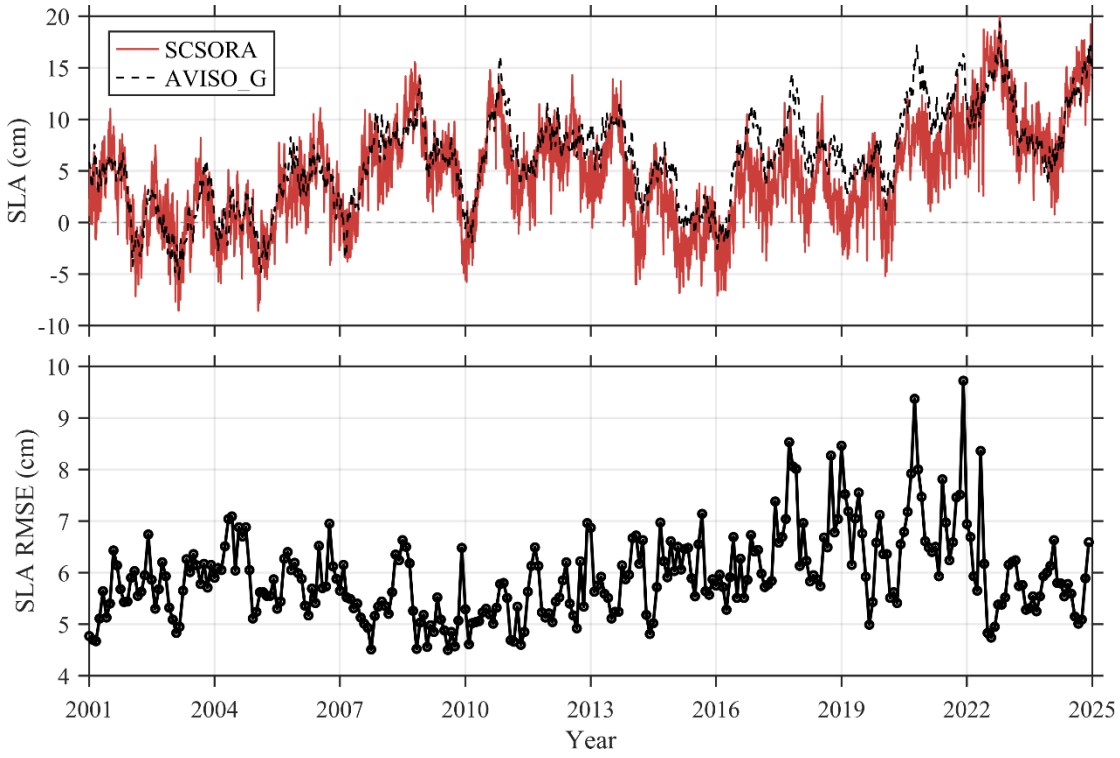


Figure 4. Time series of SLA and RMSE between the SCSORA and AVISO observations. RMSE represents the temporal deviation of the SCSORA from the observations over the same period.

6. Fig. 6: Near the coast and southern SCS south to the equator, the MLD in GLORYS is not estimated. Did you use the strictly same method to estimate the MLD in both dataset?

Response: We thank the reviewer for this comment. Upon re-confirmation, MLD was estimated using the same method for both SCSORA and GLORYS: a 0.2°C threshold criterion with a 10 m reference depth, and the temperature baseline was taken from the climatological temperature data of each dataset. No special treatment or exception was applied to either dataset. Regarding the missing MLD in GLORYS along the coast and in the southern SCS south of the equator (Figure 9, line 518), we checked the code output and confirmed that no conditions satisfying the 0.2°C threshold criterion were found in these regions, and thus no valid MLD was produced. This is most likely due to the coarser vertical resolution of GLORYS.

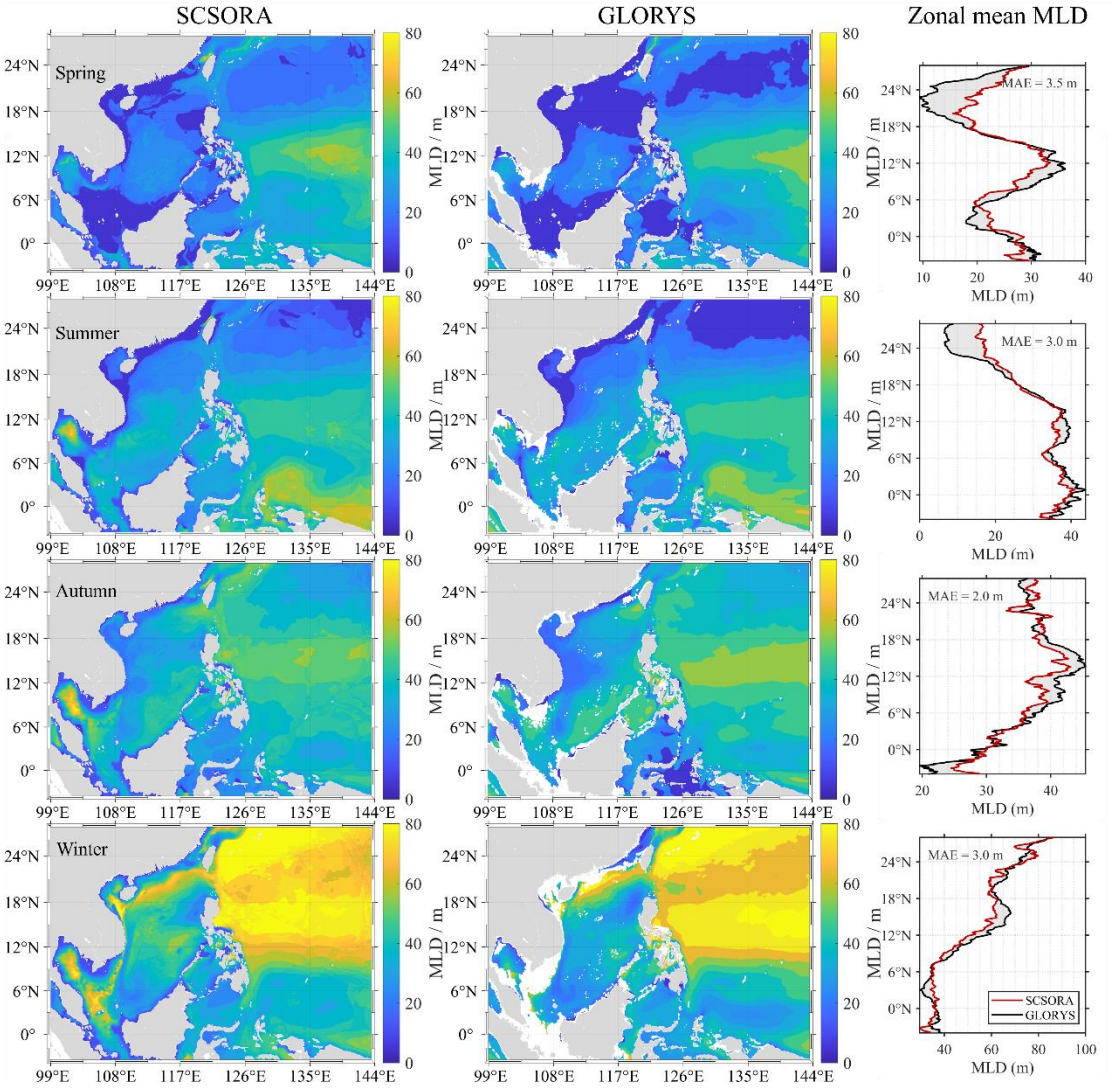


Figure 9. Seasonal climatological MLD from SCSORA (left column) and GLORYS (middle column) for spring, summer, autumn, and winter, along with the corresponding zonal mean MLD profiles (right column; red: SCSORA, black: GLORYS). The MAE of zonal mean MLD between the two products is annotated in each right panel.

7. Sec. 4.2: Could you plot or check the time series of the MHW using OISST in Fig. 10 and Fig. 11? Do these time series overlap with those using SCSORA? How the assimilated data constrains the SST in SCSORA should be checked.

Response: In the revised manuscript (Lines 712 and 736), we have added the OISST time series. In the revised Figure 15 (formerly Figure 10), the interannual time series of MHW frequency, duration, and cumulative intensity now include SCSORA, OSTIA, and OISST. In the revised Figure 16 (formerly Figure 11), the daily SST, climatology, and MHW threshold are also presented for all three products. OISST and SCSORA show broadly consistent interannual variations in MHW frequency, duration, and cumulative intensity. SCSORA reproduces the main peaks and the increasing trend evident in OISST, although slight differences exist in

amplitude at the event scale. For example, in the NWPO in 2020, OISST shows the highest peaks in MHW frequency and cumulative intensity, followed by SCSORA, while OSTIA is relatively lower. SCSORA assimilates satellite-blended OISST through the EnOI scheme of SCSOFSv2, which directly constrains the model SST. In addition, along-track SLA and Argo temperature–salinity profiles are assimilated simultaneously, constraining the upper-ocean thermal structure and further influencing SST through model dynamics and coherence relationships among them. To examine whether the agreement with OISST arises solely from assimilation, we also compared SCSORA with OSTIA, which is not assimilated. The mean RMSE between SCSORA and OSTIA is 0.357°C, comparable to the 0.340°C between SCSORA and OISST, indicating that SCSORA agrees better with OISST than that of OSTIA. In addition, the subsurface thermohaline structure is validated against independent glider and Argo observations, providing further evidence.

Changes in the manuscript:

(1) We have added the OISST time series to the revised Figure 15 (formerly Figure 10) and Figure 16 (formerly Figure 11) (Lines 712 and 736). The revised figure captions now read:

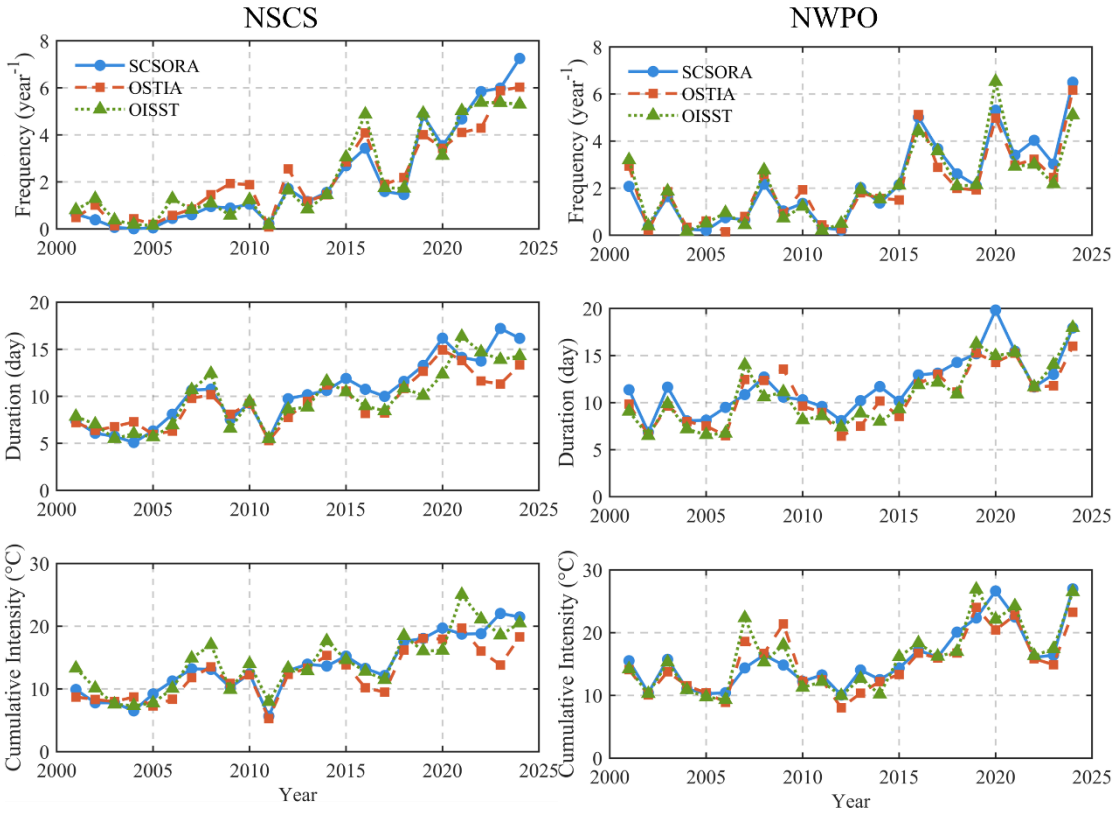


Figure 15. Interannual variability of marine heatwave (MHW) characteristics in the NSCS (left column) and the NWPO (right column) during 2001–2024, including annual frequency (top row, units: year^{-1}), mean duration (middle row, units: days), and cumulative intensity (bottom row, units: °C).

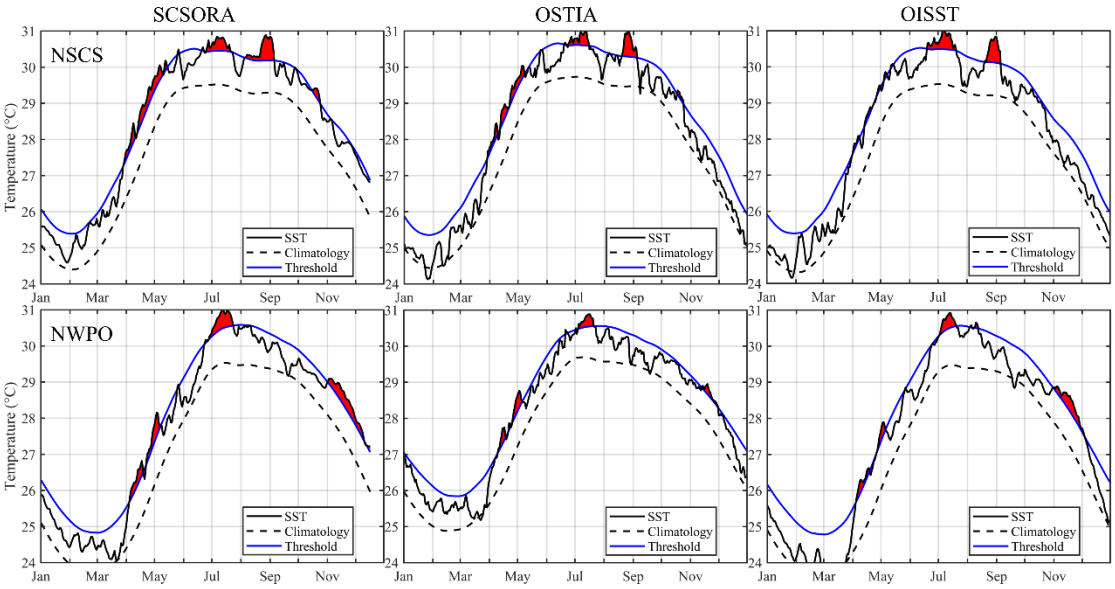


Figure 16. Seasonal evolution of area-averaged SST from SCSORA (left column), OSTIA (middle column), and OISST (right column) in the NSCS (top row) and the NWPO (bottom row) for the year 2024. Black solid lines indicate daily mean SST in 2024, black dashed lines indicate climatological mean SST, and blue solid lines indicate the MHW threshold (90th percentile of climatology). Red shading denotes marine heatwave (MHW) events where daily SST exceeds the threshold.

(2) We have added the corresponding discussion in Section 4.2 (Lines 716–735). The added text reads:

"Figure 16 presents the daily SST, climatology, and MHW thresholds based on SCSORA, OSTIA, and OISST for the NSCS and NWPO subregions in 2024, with MHW events exceeding the threshold marked by red shading. Overall, the three products exhibit a consistent seasonal cycle: SST reaches its minimum value during January–March and its peak value during June–September, while the threshold curve lies distinctly above the climatology, defining the identification criterion for MHWs (Hobday et al., 2016). In the NSCS, all three products identify significant summer MHW events, but differences exist at the event scale. The SCSORA SST time series is relatively smooth with weaker high-frequency fluctuations, resulting in longer event durations (up to 34 days) and slightly lower peak intensities (0.71°C). OSTIA is more sensitive to high-frequency variability, capable of capturing shorter events (up to 23 days), with slightly higher peak intensities (0.75°C). In the NWPO, the MHW signal is generally weaker, with lower duration and intensity; the strongest events recorded by the three products differ, with SCSORA at 0.64°C, OSTIA at 0.46°C, and OISST at 0.53°C. OISST exhibits a variation trend broadly consistent with SCSORA, but with MHW intensity and MHW duration slightly lower than those of SCSORA."

8. Sec. 4.3: Why is the number of eddies extremely large in 2022, 2023, and 2024 in SCSORA, which is not observed in AVISO (Fig 12 top panels)? Do the small-scale (submesoscale) eddies increase, which cannot be detected in AVISO?

Response: We thank the reviewer for this question. SCSORA and AVISO are generally consistent in the interannual variability of eddy counts, with both showing an increasing trend in eddy number during 2020–2023; however, the increase in SCSORA is more pronounced, and SCSORA identifies noticeably more eddies than AVISO, especially during 2022–2024. This increase may be related to the following factors. In one side, eddy activities in the SCS are modulated by the monsoon, ENSO, and PDO through local wind stress curl (Wang et al., 2003; Cheng and Qi, 2010; He et al., 2016), and the negative PDO and consecutive La Niña conditions in the 2020s may favor cyclonic eddy generation. Meanwhile, the Kuroshio intrusion through the Luzon Strait can enhance frontal and shear instability in the northern SCS, also favoring the generation of new eddies (Wu and Chiang, 2007).

In the other side, the eddy identification method itself may introduce differences of eddy counts, since the differences in effective resolution between those two datasets. Although SCSORA and AVISO employ the same velocity-vector-based identification method, their spatial resolutions differ, and the parameter choices in the method (e.g., grid-scale-related thresholds, minimum area, and maximum velocity criteria) need to be specified separately for each dataset. In this study, both datasets use A = 3 and B = 2 in common, but this parameter combination was designed for the resolution of AVISO. When applied directly to the higher-resolution SCSORA, it may lead to the identification of more small-scale eddies, thereby causing differences in eddy counts. The above phenomenon and its possible causes are also discussed in lines 742–812 of the revised manuscript.

Therefore, in subsequent research, sensitivity experiments will be designed based on SCSORA and SCSOFSv2 to investigate the mechanisms underlying the increase in eddy number during 2020–2023, including large-scale background forcing (monsoon, ENSO, PDO, and Kuroshio intrusion) and the response of eddies at different scales to this increase. In addition, identification parameters adapted to SCSORA will be developed to systematically examine the effects of identification parameters (e.g., grid-scale-related thresholds, minimum area, and maximum velocity criteria) on eddy identification results, and to analyze the differences in eddy number, size distribution, and eddy core amplitude identified under different parameter settings, so as to distinguish whether the higher eddy counts in SCSORA during 2022–2024 mainly arise from a real increase in small-scale eddies or from the capture of more small-scale eddies by the identification parameters under higher-resolution data.

Changes in the manuscript:

We have added a discussion of the possible causes of the higher eddy counts in SCSORA

during 2022–2024 in Section 4.3 (Lines 742–812). The revised text now reads:

" The statistical results indicate that in the eddy-active region of the SCS (102–122°E, 5–24°N), cyclonic eddies outnumber anticyclonic eddies (Figure. 17). SCSORA and AVISO are generally consistent in interannual variability, but SCSORA identifies a slightly higher number of eddies, especially during 2022–2024. Notably, both AVISO and SCSORA exhibit an increasing trend during 2020–2023, with a more pronounced increase in SCSORA, especially during 2022–2024. Eddy activity in the SCS is modulated by the monsoon, ENSO, and PDO through local wind stress curl (Wang et al., 2003; Cheng and Qi, 2010; He et al., 2016). The negative PDO and consecutive La Niña conditions in the 2020s may favor cyclonic eddy generation; meanwhile, the Kuroshio intrusion through the Luzon Strait can enhance frontal and shear instability in the NSCS, also favoring the generation of new eddies (Wu and Chiang, 2007). In addition, differences in effective resolution among datasets may also affect the comparison of eddy counts. Such method- and resolution-dependent discrepancies are common in eddy detection and eddy data products (Dong et al., 2025). However, the specific mechanisms can only be clarified through dedicated sensitivity experiments and validation against higher-resolution observations. In terms of seasonal variability (bottom row of Figure. 17), cyclonic eddies exhibit a bimodal distribution, with two peaks occurring in March–May and August–October, respectively. In contrast, the seasonal variability of anticyclonic eddies is weaker, manifesting only as a single broad peak in May–August."

Response to Reviewer #2:

We sincerely thank the reviewer for the constructive and insightful comments on our manuscript. We fully agree with the reviewer's general assessment that, as a data paper for ESSD, the manuscript should place greater emphasis on the validation, limitations, and added value of SCSORA, rather than on detailed process-oriented interpretations. We have therefore restructured and revised the manuscript accordingly. Specifically, we have substantially expanded the description of SCSOFSv2 in Section 2.1 to make the model configuration and data assimilation system self-contained; strengthened the validation by adding three-way comparisons for SST (SCSORA, OISST, and OSTIA) and SLA (SCSORA, AVISO_T, and AVISO_G); added spatial and seasonal distributions of SST and SLA RMSE, as well as subsurface temperature and salinity comparisons along representative sections; clarified the differences between SCSORA and existing regional reanalysis products such as REDOS; added a new validation of surface currents based on GDP drifter data; made greater use of independent glider observations for temperature–salinity and MLD validation; provided a more cautious discussion of the high-wavenumber spectral energy and the effective resolution of SCSORA; removed statements implying that SCSORA is superior to OSTIA in MHW representation; and substantially trimmed Section 4.3 so that it now serves as a concise application example rather than a detailed process-oriented interpretation. Detailed point-by-point responses are provided below, together with the corresponding changes in the revised manuscript.

1. Description of SCSOFSv2

- The description of SCSOFSv2 in Section 2.1 is currently too brief. Although the system has been documented previously in Zhu et al. (2022), readers should be able to understand the essential configuration and generation procedure of SCSORA without relying heavily on an external paper. I suggest that the authors provide a concise but sufficiently complete summary of the model configuration, SBC/OBCs, initialization or spin-up processes, major mixing parameterizations, and particularly the data assimilation configuration (ensemble construction and size, assimilation cycle and window, localization scheme, observation errors, and assimilation frequency...). In addition, if the SCSOFSv2 configuration used to produce SCSORA differs in any respect from that described in Zhu et al. (2022), these modifications should also be clearly documented.

Response: We thank the reviewer for this constructive comment. We agree that the original description of SCSOFSv2 in Section 2.1 was too brief and relied heavily on Zhu et al. (2022). Following the reviewer's suggestion, we have substantially expanded Section 2.1 to provide a concise but self-contained summary of the model configuration used to generate SCSORA, including the model code and grid, vertical coordinate, initial conditions, surface and open boundary conditions, initialization, major mixing parameterizations, and the data assimilation configuration (Lines 130–175 of the revised manuscript).

Specifically, the revised Section 2.1 now includes:

(1) Model code and grid. SCSOFSv2 is built on ROMS, a three-dimensional, nonlinear, free-surface, baroclinic ocean model based on the Reynolds-averaged Navier–Stokes equations, using a finite-difference method on an Arakawa C-grid in the horizontal direction and terrain-following σ coordinates in the vertical direction. The model domain covers the SCS and adjacent waters (99–144°E, 4.5°S–28.3°N), with a curvilinear orthogonal horizontal grid at 1/30° resolution over the SCS domain. Fifty terrain-following σ layers are used with an improved double stretching function (Shchepetkin and McWilliams, 2005), ensuring sufficient vertical resolution in the upper 300 m; the thinnest near-surface layer is about 0.09 m. The barotropic and baroclinic time steps are 5 s and 150 s, respectively.

(2) Initialization. The initial temperature and salinity fields are taken from the January monthly mean of GDEMv3 (Carnes, 2009). The model is initialized from this climatology and integrated forward; the 10-year (1991-2000) free-run daily averaged results are used to construct the background error covariance for the EnOI assimilation. The assimilation run is started since January 1st, 2001.

(3) Surface and open boundary conditions. Surface atmospheric forcing is provided by ECMWF ERA5 reanalysis (Hersbach et al., 2020) at 0.25° horizontal resolution, including 10 m wind speed, mean sea level pressure, 2 m air temperature, 2 m relative humidity, downward longwave radiation flux, precipitation rate, and shortwave radiation flux. All four lateral boundaries are opened. At the open boundaries, the Chapman (1985) condition is applied to the free surface, and the Flather (1976) radiation condition is applied to the depth-averaged barotropic velocity. The three-dimensional velocity, temperature, and salinity are treated with radiation–nudging boundary conditions following Marchesiello et al. (2001). Open-boundary values of temperature, salinity, velocity, and sea surface height are obtained by spatial interpolation of SODA 3.15.2 dataset.

(4) Mixing and advection schemes. For tracer advection, the fourth-order Akima scheme (Shchepetkin and McWilliams, 2005) is used in both horizontal and vertical directions. For momentum advection, a third-order upstream scheme is used horizontally and a fourth-order centred scheme vertically. Vertical turbulent mixing for momentum and tracers is parameterised using the Mellor–Yamada level 2.5 closure scheme (Mellor and Yamada, 1982).

(5) Data assimilation configuration. The system employs an EnOI scheme (Evensen, 2003; Oke et al., 2008) and assimilates three types of observations: satellite-derived SST, along-track satellite SLA, and in-situ Argo temperature–salinity profiles. The along-track SLA data are filtered with a Lanczos low-pass filter (cut-off wavelength 65 km, 20-day period) and are not subsampled. Observation errors are set to 3 cm for SLA (Taburet et al., 2018) and are depth-dependent for Argo profiles following Xie and Zhu (2010). The First Guess at Appropriate Time (FGAT) approach is adopted to account for asynchronous observations within the assimilation window. The background error covariance is constructed from an ensemble of model anomalies;

a Hanning low-pass filter is applied to the running mean to retain intraseasonal variability, and the anomalies are computed by subtracting the 20-day running mean from the 10-year free-run daily averaged results. The assimilation cycle is 7 days, all SLA and Argo observations within the 7-day time window, and only one day SST data before the analysis time are used in each cycle.

Changes in the manuscript:

We have substantially expanded Section 2.1 (Lines 130–175) to provide a self-contained description of the SCSOFSv2 configuration used to generate SCSORA. The revised Section 2.1 now reads as follows:

"The SCSORA dataset released in this study is generated by SCSOFSv2. SCSOFSv2 is built on the Regional Ocean Modeling System (ROMS). Its domain covers the SCS and its adjacent waters (99–144° E, 4.5° S–28.3° N). The horizontal grid is curvilinear orthogonal with a resolution of 1/30° in the SCS. The vertical coordinate uses 50 terrain-following σ layers with an improved double stretching function (Shchepetkin and McWilliams, 2005), ensuring sufficient vertical resolution within the upper 300 m to resolve the mixed layer and thermocline structure; the thinnest near-surface layer is approximately 0.09 m. The barotropic and baroclinic time steps are 5 s and 150 s, respectively.

The initial temperature and salinity fields are taken from the January monthly mean of the Generalized Digital Environmental Model version 3.0 (GDEMv3; Carnes, 2009) global climatology. The surface atmospheric forcing is provided by the ECMWF ERA5 reanalysis (Hersbach et al., 2020) at a horizontal resolution of 0.25°. The forcing variables include 10 m wind speed, mean sea level pressure, 2 m air temperature, 2 m relative humidity, downward longwave radiation flux, precipitation rate, and shortwave radiation flux. All four lateral boundaries are opened. At the open boundaries, the Chapman (1985) boundary condition is applied to the free surface, and the Flather (1976) radiation condition is applied to the depth-averaged (barotropic) velocity. The 3D velocity components, temperature, and salinity are treated using radiation–nudging boundary conditions following Marchesiello et al. (2001). The open boundary values of temperature, salinity, velocity, and SSH are obtained by spatial interpolation of SODA 3.15.2 dataset. For tracer advection, SCSOFSv2 uses the fourth-order Akima scheme (Shchepetkin and McWilliams, 2005) in both the horizontal and vertical directions. For momentum advection, a third-order upstream scheme is used in the horizontal direction and a fourth-order centred scheme in the vertical direction. Vertical turbulent mixing for both momentum and tracers is parameterised using the Mellor–Yamada level 2.5 closure scheme (Mellor and Yamada, 1982).

The system employs an EnOI data assimilation scheme (Evensen, 2003; Oke et al., 2008), assimilating three categories of observations: satellite-derived SST, along-track satellite SLA,

and in-situ temperature–salinity profiles. The along-track SLA data are filtered with a Lanczos low-pass filter (cut-off wavelength 65 km, 20-day period) and are not subsampled. Observation errors are set to 3 cm for SLA (Taburet et al., 2018) and are depth-dependent for Argo profiles following Xie and Zhu (2010). To account for asynchronous observations within the assimilation time window, the First Guess at Appropriate Time (FGAT) approach is adopted to reduce assimilation biases arising from observation timing errors. The background error covariance is constructed from an ensemble of model anomalies. A Hanning low-pass filter is applied to the running mean to retain intraseasonal variability, and the anomalies are computed by subtracting the 20-day running mean from the 10-year (1991-2000) free-run daily averaged results. The assimilation cycle is 7 days. Within each cycle, all SLA and Argo observations within the 7-day time window, and SST data 1-day before the analysis date are used. It should be noted that the number of Argo profiles in the SCS was very limited in the early 2000s and remains relatively sparse in the shallow southern SCS. To mitigate this data sparsity, the assimilation system also relies on satellite SST and along-track SLA observations, which provide better spatiotemporal coverage. In addition, the ensemble-based background error covariance allows an Argo observation to influence nearby model variables within a localization radius of 150 km."

2. Independent observation data sets

- The validation of SST and SSH/SLA would benefit from a three-way comparison among SCSORA, the observations directly assimilated into the system, and the independent or independently processed observational products used for validation. For SST, for example, OISST, SCSORA, and OSTIA could be compared together. Similarly, the assimilated along-track altimeter, SCSORA, and gridded AVISO could be examined for SSH/SLA. Such comparisons would help clarify (1) how closely the reanalysis follows the assimilated observations, (2) whether the resulting variability is also consistently reproduced in the independent validation product, (3) whether discrepancies between the two observational products themselves may be contributing to what is currently interpreted as model bias or error. This distinction is particularly important because the validation products are not fully independent from the observational systems used in the assimilation.

Response: As suggested, we have expanded the validation work in Section 3 by adding three-way comparisons for both SST and SLA. Regarding SST, SCSORA is now compared with both OISST and OSTIA. The revised Section 3.1 (Line 338 of the revised manuscript, Figure 2) shows that the SST trend patterns and interannual variability reproduced by SCSORA are consistent with both OSTIA and OISST. The three datasets exhibit highly consistent SST anomaly variations, including the pronounced warm anomalies associated with the 2009–2010 El Niño and the marked warming during 2023–2024. The mean RMSE between SCSORA and OSTIA is 0.357°C, and that between SCSORA and OISST is 0.340°C. The RMSE of SCSORA relative to OISST and OSTIA is highly similar in both spatial and seasonal distributions (Figure.

3, line 381), indicating systematic biases relative to satellite SST products in coastal, shelf, and strong-gradient regions. These regions are influenced by complex dynamical processes such as monsoon-driven coastal circulation and local upwelling, which pose certain challenges to model simulation.

Regarding SLA, we have added comparisons of SCSORA with along-track AVISO (AVISO_T) and gridded AVISO (AVISO_G) in the revised Section 3.2 (Lines 401-410 of the revised manuscript), together with the corresponding spatial and seasonal distributions of SLA RMSE (Figure. 5, line 414). The results show that the spatial and seasonal distributions of RMSE for SCSORA relative to AVISO_T and AVISO_G are generally consistent. RMSE is relatively low in the open waters of the central and southern SCS, mostly below 5 cm, while larger errors occur in the Luzon Strait, around Taiwan Island, and in the westward-extending northwestern Pacific, locally exceeding 10 cm.

In summary, the errors between SCSORA and satellite observations are low and stable, indicating that the SCSORA is effectively constrained by the assimilation system and can closely track the assimilated satellite observational information; however, the similarity in RMSE distributions also reflects that SCSORA exhibits certain systematic biases relative to satellite observational products in coastal, shelf, strong-gradient, and strong-current regions.

Changes in the manuscript:

(1) We have added the OISST SST anomaly time series and the three-way comparison in Section 3.1 (Line 338). The revised Figure 2 caption now reads:

"

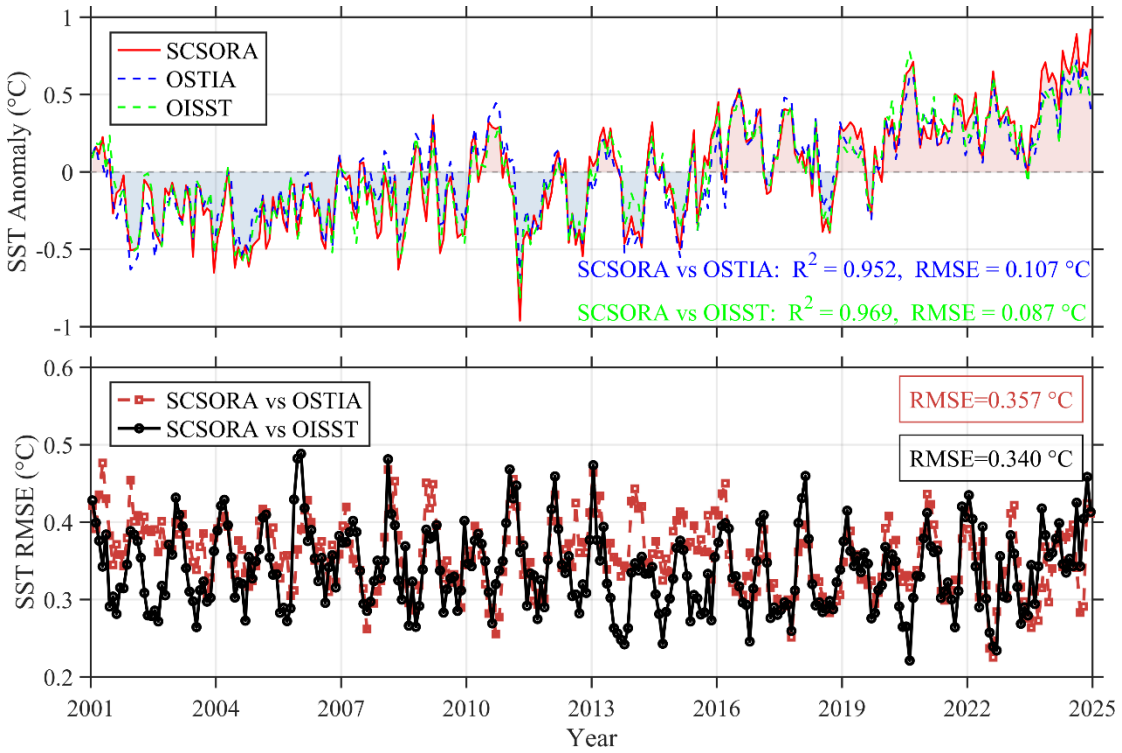


Figure 2. Time series of SST anomalies and RMSE relative to the 2001–2024 SST climatology. Comparisons are shown among SCSORA, OSTIA, and OISST. SST anomalies are computed as daily departures from the 2001–2024 climatological mean SST. "

(2) We have added the seasonal spatial distributions of SST RMSE between SCSORA and OISST (top row) and between SCSORA and OSTIA (bottom row) as Figure 3 (Line 381). The revised Figure 3 caption now reads:

"

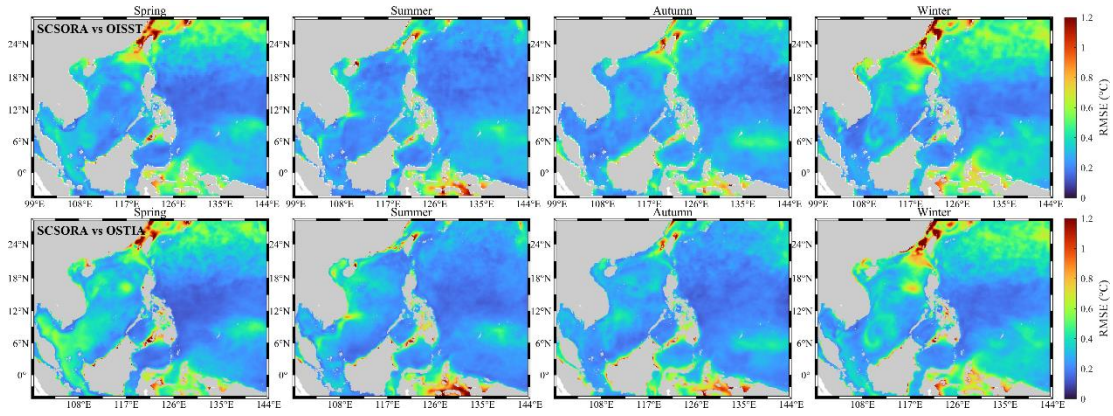


Figure 3. Seasonal spatial distributions of SST RMSE between SCSORA and OISST (top row) and between SCSORA and OSTIA (bottom row) for spring, summer, autumn, and winter (from left to right). "

(3) We have added the corresponding discussion in Section 3.1 (Lines 354–380). The

added text reads:

" The RMSE of SST between SCSORA and both OISST and OSTIA exhibits pronounced regional disparities and seasonal evolution (Figure 3). Overall, the RMSE in the central open waters of the SCS is generally below 0.5°C, whereas larger errors are predominantly distributed in the Taiwan Strait, the northern SCS continental shelf, and certain coastal regions, with localized values exceeding 0.8°C. Such spatial discrepancies may be associated with complex ocean dynamical processes in nearshore and shelf seas, such as monsoon-driven coastal circulations, tidal mixing, and local upwelling.

In terms of seasonal variability, the RMSE increases markedly during winter in the northern SCS and adjacent to the Taiwan Strait, forming a relatively prominent high-error region. Previous studies have demonstrated that the northeasterly monsoon can drive the southward transport of cold coastal water and generate a distinct SST front in the Taiwan Strait; concurrently, intensified wintertime sea surface cooling in the northern SCS further enhances the regional temperature gradient (Kuo et al., 2018). Therefore, the relatively large RMSE in these regions may be attributed to model biases in simulating monsoon-driven sea surface heat fluxes, coastal water mass transport, and the positioning of temperature fronts. As the northeasterly monsoon gradually weakens, the high-error extent in the northern SCS diminishes accordingly. During summer, the central open waters of the SCS maintain relatively low RMSE, yet a localized high-value band emerges along the Vietnam coast. Xie et al. (2003) noted that the southwesterly monsoon can drive coastal upwelling off Vietnam and promote the offshore expansion of cold water through local wind stress curl and anticyclonic circulation. These processes may intensify the local SST spatial gradient, rendering the simulated results in this region more sensitive to the accuracy of wind fields, vertical mixing, and horizontal advection. Nevertheless, SCSORA is capable of reproducing SST over most of the SCS reasonably well across all seasons, particularly exhibiting low RMSE in open waters, which indicates its favorable capability for SST reconstruction."

(4) We have added the comparisons of SCSORA with AVISO_T and AVISO_G in Section 3.2 (Lines 401–410) and the corresponding seasonal spatial distributions of SLA RMSE as Figure 5 (Line 414). The revised Figure 5 caption now reads:

"

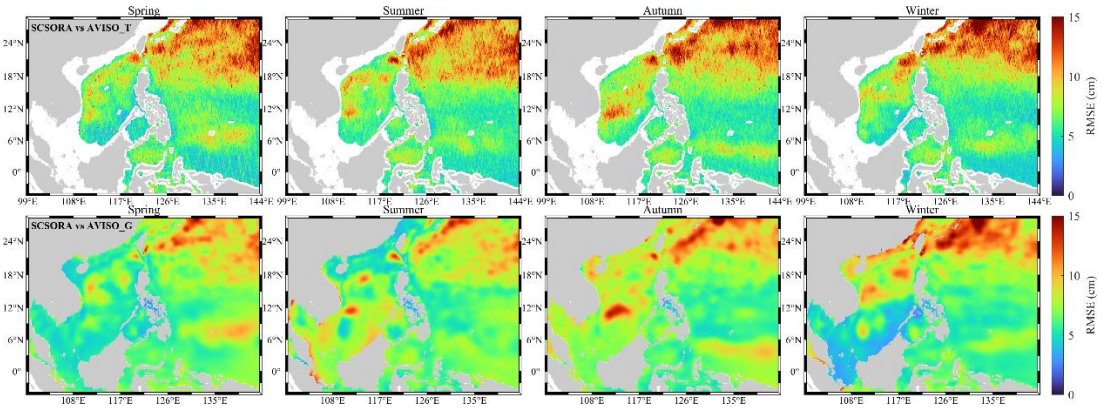


Figure 5. Seasonal spatial distributions of SLA root mean square error (RMSE) between SCSORA and AVISO_T data (top row) and AVISO_G data (bottom row) for spring, summer, autumn, and winter (from left to right). "

(5) We have added the corresponding discussion in Section 3.2 (Lines 401–410). The added text reads:

"The RMSE of SLA between SCSORA and both along-track (AVISO_T) and gridded (AVISO_G) AVISO products exhibits pronounced spatial disparities and seasonal variability (Figure 5). The RMSE is relatively low in the central and southern open waters of the SCS, with values below 5 cm over most of the region, whereas larger errors are primarily distributed in the Luzon Strait, the vicinity of Taiwan and the northwestern Pacific to the east thereof, where localized values exceed 10 cm. These regions also exhibit relatively higher errors across different seasons. These areas are significantly influenced by the Kuroshio and mesoscale eddy activities, characterized by strong SSH variability (Nan et al., 2015). Therefore, the relatively large RMSE may be attributed to model biases in simulating Kuroshio path variability, eddy activity, and the associated SSH gradients. Nevertheless, in general, SCSORA exhibits relatively low RMSE against both AVISO datasets over most of the open waters of the SCS, although considerable discrepancies remain in regions with intense Kuroshio and mesoscale eddy activity. "

3. Spatial pattern validation

- The current SST (Fig. 2) and SSH/SLA (Fig. 3) evaluations are largely focused on temporal variations and domain-averaged statistics. Given the high spatial resolution and regional nature of SCSORA, I suggest that the authors also provide spatial evaluations of the reanalysis performance, for example, maps of bias, RMSE, and correlations. For the subsurface fields, comparisons of temperature and salinity distributions along representative vertical sections would also provide a more direct assessment of how well SCSORA reproduces the observed 3-D ocean structure.

Response: We agree that an evaluation based solely on temporal variability and regionally averaged statistics is insufficient to fully reflect the reanalysis performance of SCSORA at high

spatial resolution. To this end, we have added spatial evaluations of SST and SLA in the revised manuscript, together with additional subsurface temperature and salinity comparisons along representative sections.

Regarding SST (Lines 354–380 of the revised manuscript), we have added spatial and seasonal distributions of RMSE between SCSORA and both OISST and OSTIA (Figure. 3, line 381). The results show that RMSE is generally below 0.5°C in the open waters of the central SCS, while it locally exceeds 0.8°C in the Taiwan Strait, the northern SCS shelf, and some coastal regions. In winter, RMSE increases in the northern SCS and near the Taiwan Strait, whereas in summer a localized high-value band appears along the Vietnam coast. These spatial and seasonal characteristics are related to complex dynamical processes such as monsoon-driven coastal circulation, and local upwelling, indicating that SCSORA performs well in open waters but still faces challenges in coastal and shelf regions.

Regarding SLA (Lines 401–410 of the revised manuscript), we have added spatial and seasonal distributions of RMSE between SCSORA and along-track AVISO (AVISO_T) and gridded AVISO (AVISO_G), respectively (Figure 5, line 411). The results show that RMSE is relatively low in the open waters of the central and southern SCS, mostly below 5 cm, while larger errors occur in the Luzon Strait, around Taiwan Island, and the westward-extending northwestern Pacific Ocean, locally exceeding 10 cm. These regions are significantly influenced by the Kuroshio and intense mesoscale eddy activities. The RMSE distributions of SCSORA relative to the two AVISO products are generally consistent, reflecting systematic biases in strong-current and strong-eddy regions.

For the validation of subsurface fields, we have added comparisons of the vertical distributions of temperature and salinity along representative sections between SCSORA and glider observations (Figure. 8, line 478 of the revised manuscript). The results show that SCSORA can reproduce the thermocline position and the main vertical gradients reasonably, with temperature biases in most water layers keeping within ±1.5°C; salinity ranges are approximately 34–35 PSU, in good agreement with observations, and errors decrease with depth increasing. Below 300 m, the salinity structure shows high consistency in most years, whereas the upper layer exhibits greater dispersion, with anomalously high surface salinity in individual years. It should be noted that SCSORA is a daily averaged product and is smoother than glider observations; therefore, local vertical undulations of the thermocline and upper ocean, as well as short-timescale temperature and salinity anomalies, are noticeably weakened in SCSORA, which may be related to the smoothing of high-frequency signals by daily averaging.

In summary, the newly added spatial RMSE maps of SST, SLA, and the temperature–salinity comparisons along sections allow a more direct assessment of the ability of SCSORA to reproduce the three-dimensional ocean structure of the SCS, and compensate for the

limitation of the original manuscript, which relied solely on temporal variability and regionally averaged statistics.

Changes in the manuscript:

(1) We have added the seasonal spatial distributions of SST RMSE between SCSORA and OISST (top row) and between SCSORA and OSTIA (bottom row) as Figure 3 (Line 381). The revised Figure 3 caption now reads:

"

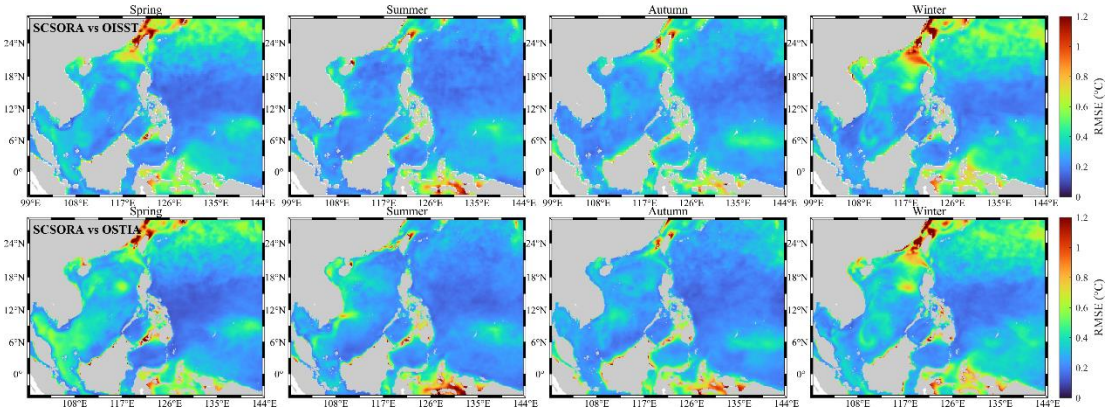


Figure 3. Seasonal spatial distributions of SST RMSE between SCSORA and OISST (top row) and between SCSORA and OSTIA (bottom row) for spring, summer, autumn, and winter (from left to right)."

(2) We have added the comparisons of SCSORA with AVISO_T and AVISO_G in Section 3.2 and the corresponding seasonal spatial distributions of SLA RMSE as Figure 5 (Line 411). The revised Figure 5 caption now reads:

"

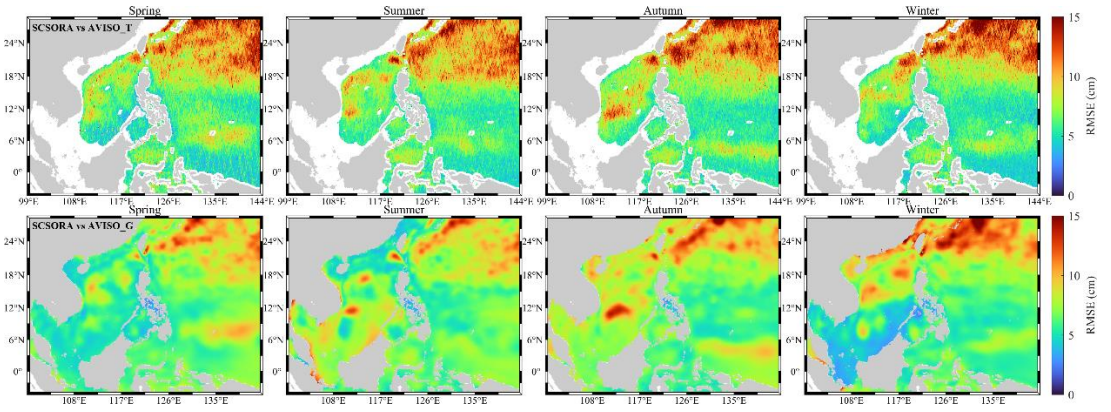


Figure 5. Seasonal spatial distributions of SLA root mean square error (RMSE) between SCSORA and AVISO_T data (top row) and AVISO_G data (bottom row) for spring, summer, autumn, and winter (from left to right)."

(3) We have added comparisons of the vertical distributions of temperature and salinity along representative sections between UG observations and SCSORA in Section 3.3 (Line 478) as Figure 8. The figure caption reads:

"

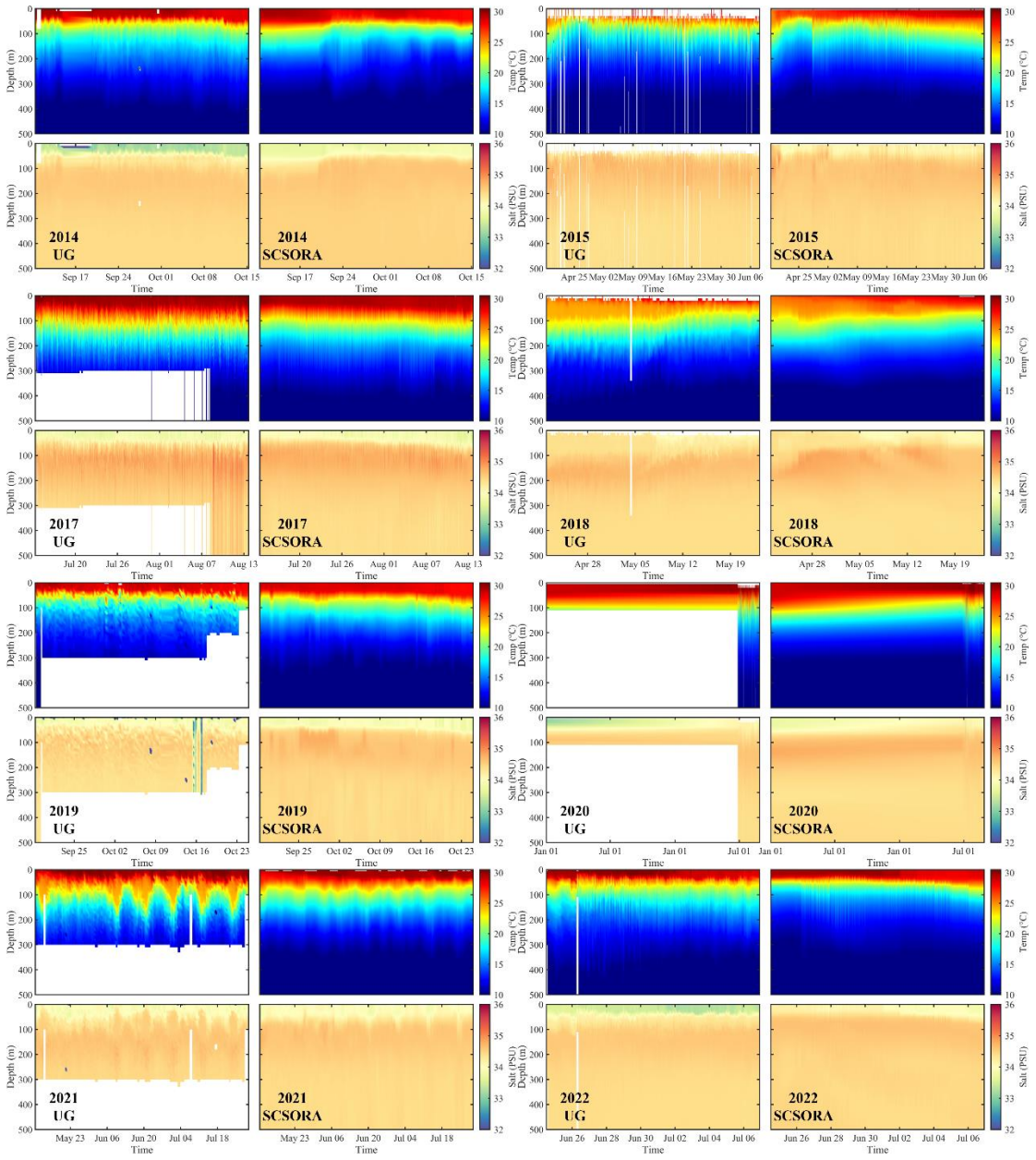


Figure 8. Comparison of vertical section time series of temperature (upper panels) and salinity (lower panels) between UG observations (left column) and SCSORA products (right column) from 2014 to 2022. "

(4) We have added the corresponding discussion of the spatial and seasonal patterns of SST and SLA RMSE, as well as the subsurface temperature–salinity comparisons, in Sections 3.1–3.3 (Lines 354–380, 401–410, and 455–477). The added text includes:

"The RMSE of SST between SCSORA and both OISST and OSTIA exhibits pronounced regional disparities and seasonal evolution (Figure 3). Overall, the RMSE in the central open waters of the SCS is generally below 0.5°C, whereas larger errors are predominantly distributed in the Taiwan Strait, the northern SCS continental shelf, and certain coastal regions, with localized values exceeding 0.8°C. Such spatial discrepancies may be associated with complex ocean dynamical processes in nearshore and shelf seas, such as monsoon-driven coastal circulations, tidal mixing, and local upwelling.

In terms of seasonal variability, the RMSE increases markedly during winter in the northern SCS and adjacent to the Taiwan Strait, forming a relatively prominent high-error region. Previous studies have demonstrated that the northeasterly monsoon can drive the southward transport of cold coastal water and generate a distinct SST front in the Taiwan Strait; concurrently, intensified wintertime sea surface cooling in the northern SCS further enhances the regional temperature gradient (Kuo et al., 2018). Therefore, the relatively large RMSE in these regions may be attributed to model biases in simulating monsoon-driven sea surface heat fluxes, coastal water mass transport, and the positioning of temperature fronts. As the northeasterly monsoon gradually weakens, the high-error extent in the northern SCS diminishes accordingly. During summer, the central open waters of the SCS maintain relatively low RMSE, yet a localized high-value band emerges along the Vietnam coast. Xie et al. (2003) noted that the southwesterly monsoon can drive coastal upwelling off Vietnam and promote the offshore expansion of cold water through local wind stress curl and anticyclonic circulation. These processes may intensify the local SST spatial gradient, rendering the simulated results in this region more sensitive to the accuracy of wind fields, vertical mixing, and horizontal advection. Nevertheless, SCSORA is capable of reproducing SST over most of the SCS reasonably well across all seasons, particularly exhibiting low RMSE in open waters, which indicates its favorable capability for SST reconstruction."

"The RMSE of SLA between SCSORA and both along-track (AVISO_T) and gridded (AVISO_G) AVISO products exhibits pronounced spatial disparities and seasonal variability (Figure 5). The RMSE is relatively low in the central and southern open waters of the SCS, with values below 5 cm over most of the region, whereas larger errors are primarily distributed in the Luzon Strait, the vicinity of Taiwan and the northwestern Pacific to the east thereof, where localized values exceed 10 cm. These regions also exhibit relatively higher errors across different seasons. These areas are significantly influenced by the Kuroshio and mesoscale eddy activities, characterized by strong SSH variability (Nan et al., 2015). Therefore, the relatively large RMSE may be attributed to model biases in simulating Kuroshio path variability, eddy activity, and the associated SSH gradients. Nevertheless, in general, SCSORA exhibits relatively low RMSE against both AVISO datasets over most of the open waters of the SCS, although considerable discrepancies remain in regions with intense Kuroshio and mesoscale

eddy activity."

" SCSORA is capable of reproducing the temperature and salinity distribution characteristics along the UG observational sections reasonably well (Figure 8). In terms of temperature, SCSORA is generally consistent with the observed thermocline position and major vertical gradients in most years. The surface temperature is approximately 28–30°C, with a pronounced temperature decrease within the depth range of roughly 50–200 m. Combined with the temperature bias statistics, the mean temperature bias within most of the water column is constrained to within ±1.5°C, with the error dispersion generally decreasing below 200 m, indicating that SCSORA exhibits favourable stability in reproducing subsurface temperature structure. With respect to salinity, both datasets display relatively comparable vertical distributions across most observational depths, with salinity ranging from 34 to 35 PSU. Compared with temperature, salinity discrepancies are generally smaller, and the errors diminish with increasing depth. Below 300 m, the salinity structure exhibits high consistency in most years; however, the dispersion in the upper ocean is relatively larger, with localized salinity overestimation occurring in certain years (e.g., 2014, 2020, 2022). It should be noted that the SCSORA data are daily-averaged products, which are inherently smoother than the UG observations; consequently, the localized vertical undulations within the thermocline and upper ocean, as well as short-timescale temperature and salinity anomalies present in the observations, are markedly attenuated in SCSORA. This phenomenon is associated with the smoothing of high-frequency signals induced by daily averaging and tidal mixing missed in SCSOFSv2."

4. Comparison with previous regional reanalysis data

- The manuscript would benefit from a clearer discussion of how SCSORA differs from previously available regional reanalysis products for the South China Sea (ex. https://www.nature.com/articles/sdata201452) in Introduction.

Response: Existing global ocean reanalysis products (e.g., GLORYS and HYCOM), although providing three-dimensional temperature, salinity, and velocity fields, typically have spatial resolutions of 1/4° to 1/12°. For the SCS, where mesoscale to sub-mesoscale eddy activities are intense, these products struggle to accurately resolve mesoscale eddy structures, and their data assimilation schemes are not optimized for the local dynamical characteristics of the SCS. Regional reanalysis efforts for the SCS have been carried out previously. Zeng et al. (2014) developed REDOS based on ROMS and a multiscale incremental 3DVAR scheme, with a horizontal resolution of 0.1° and a temporal span of 19 years (1992–2010). REDOS assimilated along-track SLA and in-situ temperature and salinity profiles, and used the then-available reanalysis fields as atmospheric forcing and lateral boundary conditions, providing three-dimensional temperature, salinity, and velocity fields for the SCS. This work represents an important early advance in regional ocean reanalysis for the SCS and laid an important foundation for subsequent studies.

Building on this, the SCSORA generated in this study differs from existing regional reanalysis products for the SCS, such as REDOS, in the following aspects: first, it has a longer temporal span, covering 24 years from 2001 to 2024 and being updated at irregular intervals; second, it has a higher horizontal resolution of 1/30°, which is more conducive to resolving mesoscale eddy structures in the SCS; third, it assimilates a richer set of observations, including satellite SST, along-track SLA, and numerous Argo in-situ temperature and salinity profiles; fourth, it adopts an EnOI assimilation scheme and uses ERA5 and SODA 3.15.2 to provide atmospheric forcing and open boundary conditions, and is capable of simultaneously providing three-dimensional temperature, salinity, and velocity fields as well as sea surface variables. Therefore, SCSORA represents a clear improvement and extension over existing regional reanalysis products for the SCS in terms of temporal span, spatial resolution, number of assimilated observations, and completeness of output variables. We have added relevant discussion on previous regional reanalysis efforts and their limitations in the revised manuscript (Lines 85–99).

Changes in the manuscript:

We have added a discussion in the Introduction (Lines 85–99) comparing SCSORA with previously available regional reanalysis products for the South China Sea, particularly REDOS (Zeng et al., 2014). The added text reads:

" Regional reanalysis efforts targeting the SCS have already been undertaken. Zeng et al. (2014) developed REDOS, a daily reanalysis product based on ROMS and a multi-scale incremental 3DVAR scheme, with a horizontal resolution of 0.1° and a temporal span of 19 years (1992–2010). It assimilated along-track SLA and in-situ temperature and salinity profiles and adopted the then-available reanalysis fields as atmospheric forcing and lateral boundary conditions, providing 3D temperature, salinity, and current fields for the SCS over that period. This work represented an important early advance in regional ocean reanalysis for the SCS and has laid a significant foundation for subsequent studies. On this basis, there is clear research need to further develop a regional reanalysis product with a longer temporal span, more abundant assimilated data, and the capability to simultaneously provide 3D temperature, salinity, and current fields as well as sea surface height.

Based on the above needs, the present study proposes a long-term, high-resolution 3D South China Sea Ocean Reanalysis (SCSORA) dataset, which is built upon the second version of the SCS Operational Oceanography Forecast System (SCSOFSv2, Zhu et al., 2022). SCSOFSv2 employs an Ensemble Optimal Interpolation (EnOI) assimilation scheme to assimilate satellite-blended SST, along-track SLA, and a larger number of Argo in-situ temperature–salinity profile observations and provides a complete 24-year (2001–2024) daily mean dataset including 3D temperature, salinity, and current velocity fields, as well as 2D sea surface height (SSH)."

5. Validation of circulation

- Although SCSORA provides 3-D current velocity fields, the validation of the circulation is limited. I suggest including additional validation metrics for the regional circulation and/or volume transport through key straits, where appropriate estimates are available.

Response: As suggested, we have added Section 3.5 on the validation of surface currents based on GDP drifting buoy data in lines 537–582 of the revised manuscript.

Specifically, we first selected typical GDP drifting buoy trajectories and qualitatively compared them with the contemporaneous SCSORA surface current field and SLA (Figure. 11). The results show that the GDP trajectories are generally consistent with the simulated flow direction and speed variations; most trajectories evolve along the direction of the simulated flow field and are consistent with SLA gradients and closed contour structures. In regions of intense mesoscale eddy activity, the GDP trajectories can reflect the rotational characteristics of eddies; in the Luzon Strait and its adjacent waters, both the GDP trajectories and the analyzed flow field exhibit strong current structures.

On this basis, we further conducted a quantitative validation of the SCSORA surface current speed based on SCS GDP data from 2001 to 2024 (Table 2). A total of 174696 valid GDP samples were obtained over the 24 years. The results show that the SCSORA surface current speed errors are generally stable: the monthly-scale RMSE of the U component is 16.57–18.23 cm/s, with a mean of 17.21 cm/s; that of the V component is 16.05–17.70 cm/s, with a mean of 16.73 cm/s; and that of the current speed magnitude is 14.45–16.59 cm/s, with a mean of 15.50 cm/s. The inter-monthly variation ranges of all three metrics are relatively narrow, indicating that the surface current speed errors do not exhibit pronounced seasonal abrupt changes. Overall, SCSORA can reasonably reproduce the main spatial structure and seasonal variation characteristics of the SCS surface current field, but the RMSE of 15–17 cm/s also indicates that the model still has certain uncertainties in the precise characterization of the absolute magnitude of local current speeds.

Changes in the manuscript:

We have added a new subsection, Section 3.5, on the validation of surface currents based on GDP drifting buoy data (Lines 537–582). The added text includes the qualitative comparison of GDP trajectories with the SCSORA surface current field and SLA, and the quantitative validation of surface current speed.

"

Since current observations are relatively scarce compared with temperature, salinity, and SLA, and surface velocity is readily influenced by wind-driven drift and mesoscale processes, we first conducted a qualitative validation of the surface current field through the spatial

correspondence between representative GDP trajectories and the SCSORA surface current field and SLA. Figure 11 presents several typical GDP observational cases alongside the contemporaneous SCSORA-simulated surface current field and SLA distribution. Overall, the GDP trajectories show good consistency with the simulated flow direction and velocity variations, most trajectories evolving along the direction of the simulated current field and aligning with the corresponding SLA gradients and closed contour structures. In regions of intense mesoscale eddy activities, the GDP trajectories are able to reflect the rotational characteristics of eddies. In the Luzon Strait and its adjacent waters, both the GDP trajectories and the simulated current field exhibit strong flow structures, demonstrating that SCSORA possesses a certain capability in characterizing the Kuroshio intrusion and associated circulation features. It should be noted that localized offsets between trajectories and simulated flow directions still exist (Figure 11c), which may be related to the wind drift effect on drifting buoys, spatiotemporal sampling differences between GDP and the model, and local small-scale processes.

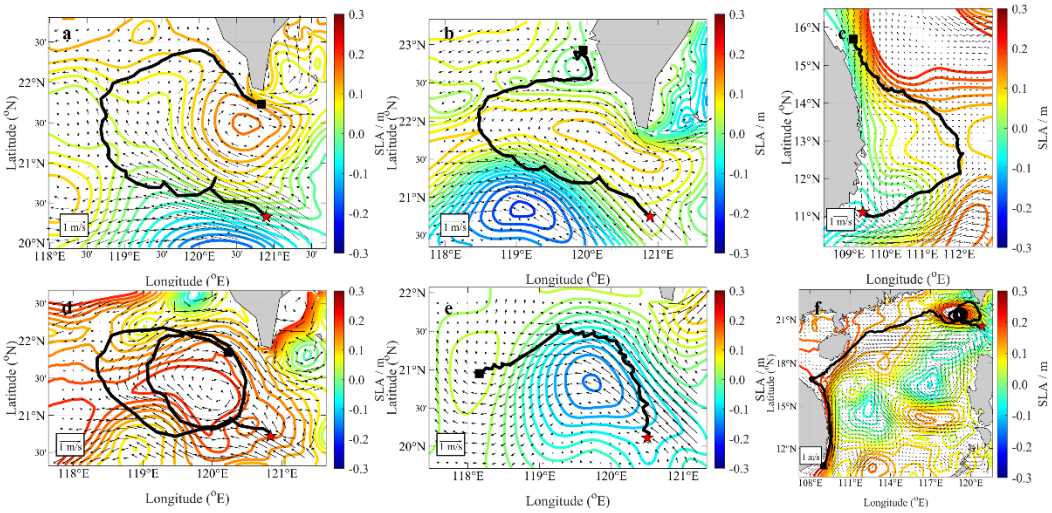


Figure 11. Comparison between the SCSORA surface current field and drifting buoy trajectories. The thick black lines denote drifting buoy trajectories originating from the red stars; the arrows (units: m/s) and contours (units: m) represent the SCSORA surface current field and SLA, respectively.

On this basis, a quantitative comparison of the SCSORA surface velocity was further conducted on a monthly basis using GDP data from the SCS for the period 2001–2024 (Table 2). A total of 174696 valid GDP samples were obtained over the 24-year period. The monthly-scale root-mean-square differences (RMSD) calculated from contemporaneous samples over the 24 years indicates that the SCSORA surface velocity error is generally stable. The 12-month RMSD of the U component ranges from 16.57 to 18.23 cm s^{-1}, with a mean of 17.21 cm s^{-1}, being largest in April (18.23 cm s^{-1}) and smallest in September (16.57 cm s^{-1}); the RMSD of the V component ranges from 16.05 to 17.70 cm s^{-1}, with a mean of 16.73 cm s^{-1}, being largest

in May (17.70 cm s^{-1}) and smallest in January (16.05 cm s^{-1}). The RMSD of the current speed ranges from 14.45 to 16.59 cm s^{-1}, with a mean of 15.50 cm s^{-1}, being smallest in August (14.45 cm s^{-1}) and largest in December (16.59 cm s^{-1}). The 12-month RMSD ranges of the three metrics are all relatively narrow, with the intermonthly ranges of the U component, V component, and current speed being 1.66, 1.65, and 2.14 cm s^{-1}, respectively, indicating that the surface velocity error derived from the long-term sample statistics for 2001–2024 does not exhibit pronounced seasonal abrupt changes.

Overall, the mean RMSD of the SCSORA surface U component, V component, and current speed for 2001–2024 are 17.21, 16.73, and 15.50 cm s^{-1}, respectively, with relatively limited error variation among different months. Combined with the consistency between the GDP trajectories and the simulated current field in terms of major circulation structures, SCSORA is able to reproduce the main spatial structure of the SCS surface current field and its seasonal variation characteristics reasonably. Meanwhile, the RMSD of approximately 15–17 cm s^{-1} also indicates that, although the model can adequately describe the major circulation and mesoscale structures, certain uncertainties remain in the precise characterization of the absolute magnitude of local current velocities. Therefore, the SCSORA surface current field can serve as a background flow field for studies of multi-scale ocean processes in the SCS; however, for applications highly sensitive to absolute velocity magnitudes, further evaluation in conjunction with independent observations or higher-resolution data is still warranted.

Table 2. Climatological monthly root-mean-square differences (RMSD) between drifting buoy velocities and SCSORA velocities.

Month	Observation Number	RMSD of U (cm s^{-1})	RMSD of V (cm s^{-1})	RMSD of velocity magnitude (cm s^{-1})
1	24191	16.95	16.05	15.79
2	17200	17.17	16.52	15.92
3	14802	17.37	16.71	15.55
4	10223	18.23	17.47	15.84
5	11694	17.69	17.70	15.63
6	11384	17.88	17.25	14.84
7	11513	17.27	16.98	15.02
8	10353	16.86	16.09	14.45

9	9716	16.57	16.42	14.88
10	14042	16.86	16.28	15.39
11	17026	16.76	16.49	16.06
12	22552	16.97	16.82	16.59
mean	14558	17.21	16.73	15.50

"

6. Use of glider data

- Since the Argo profiles are assimilated into SCSORA, their comparison mainly represents analysis-observation consistency rather than independent validation. I suggest making greater use of the independent glider observations, for example by comparing vertical sections of temperature and salinity. The glider data could also be used for MLD validation, while retaining the current GLORYS comparison to assess consistency between reanalysis products.

Response: As suggested by the reviewer, we have added glider data from 2014 and 2022 in the revised manuscript and strengthened the use of independent glider observations to validate temperature–salinity vertical profiles and MLD, while retaining the comparison with GLORYS to assess consistency among reanalysis products.

Specifically, we have added comparisons of the vertical distributions of temperature and salinity along representative sections between glider observations and SCSORA for 2014–2022 (Lines 455–480 of the revised manuscript). The results show that SCSORA can reproduce the thermocline position and the main vertical gradients reasonably. Surface temperature is approximately 28–30°C, with pronounced cooling occurring at depths of about 50–200 m. Combined with the temperature bias statistics, the mean temperature bias for most of the water column is kept within ±1.5°C, and the error dispersion generally decreases below 200 m, indicating that SCSORA has good stability in reproducing subsurface temperature structures. In terms of salinity, the vertical distributions of the two datasets are relatively close at most observation depths, with salinity ranging approximately from 34 to 35 PSU; compared with temperature, salinity differences are generally smaller, and errors decrease with increasing depth. Below 300 m, the salinity structure shows high consistency in most years, whereas the upper layer exhibits greater dispersion, with locally high salinity in individual years (e.g., 2014, 2020, and 2022). It should be noted that SCSORA is a daily averaged product and is inherently smoother than glider observations; therefore, local vertical undulations of the thermocline and upper ocean, as well as short-timescale temperature and salinity anomalies, are noticeably weakened in SCSORA, which may be related to the smoothing of high-frequency signals by daily averaging.

In addition, we used glider data to further evaluate the ability of SCSORA to reproduce the vertical mixing structure of the upper ocean in the SCS (Lines 527-535 of the revised manuscript). We calculated the annual mean bias between the MLD derived from glider observations and that from SCSORA. The results show that, except for 2014, when the bias is close to 0 m, the MLD biases in the remaining years are all negative, indicating that the mixed layer simulated by SCSORA is generally deeper than that observed by gliders. Among these, the biases are most pronounced in 2017, 2018, and 2022, with mean biases of approximately −6.4, −6.1, and −6.9 m, respectively; the biases in 2019–2021 are relatively small, approximately −3.6 to −4.4 m. The interannual variation of the median bias is highly consistent with that of the mean bias. At the same time, we have retained the comparison with GLORYS to assess consistency among reanalysis products.

Changes in the manuscript:

(1) We have added comparisons of the vertical distributions of temperature and salinity along representative sections between UG glider observations and SCSORA in Section 3.3 (Lines 455–480) as Figure 8.

"SCSORA is capable of reproducing the temperature and salinity distribution characteristics along the UG observational sections reasonably well (Figure 8). In terms of temperature, SCSORA is generally consistent with the observed thermocline position and major vertical gradients in most years. The surface temperature is approximately 28–30°C, with a pronounced temperature decrease within the depth range of roughly 50–200 m. Combined with the temperature bias statistics, the mean temperature bias within most of the water column is constrained to within ±1.5°C, with the error dispersion generally decreasing below 200 m, indicating that SCSORA exhibits favourable stability in reproducing subsurface temperature structure. With respect to salinity, both datasets display relatively comparable vertical distributions across most observational depths, with salinity ranging from 34 to 35 PSU. Compared with temperature, salinity discrepancies are generally smaller, and the errors diminish with increasing depth. Below 300 m, the salinity structure exhibits high consistency in most years; however, the dispersion in the upper ocean is relatively larger, with localized salinity overestimation occurring in certain years (e.g., 2014, 2020, 2022). It should be noted that the SCSORA data are daily-averaged products, which are inherently smoother than the UG observations; consequently, the localized vertical undulations within the thermocline and upper ocean, as well as short-timescale temperature and salinity anomalies present in the observations, are markedly attenuated in SCSORA. This phenomenon is associated with the smoothing of high-frequency signals induced by daily averaging and tidal mixing missed in SCSOFSv2.

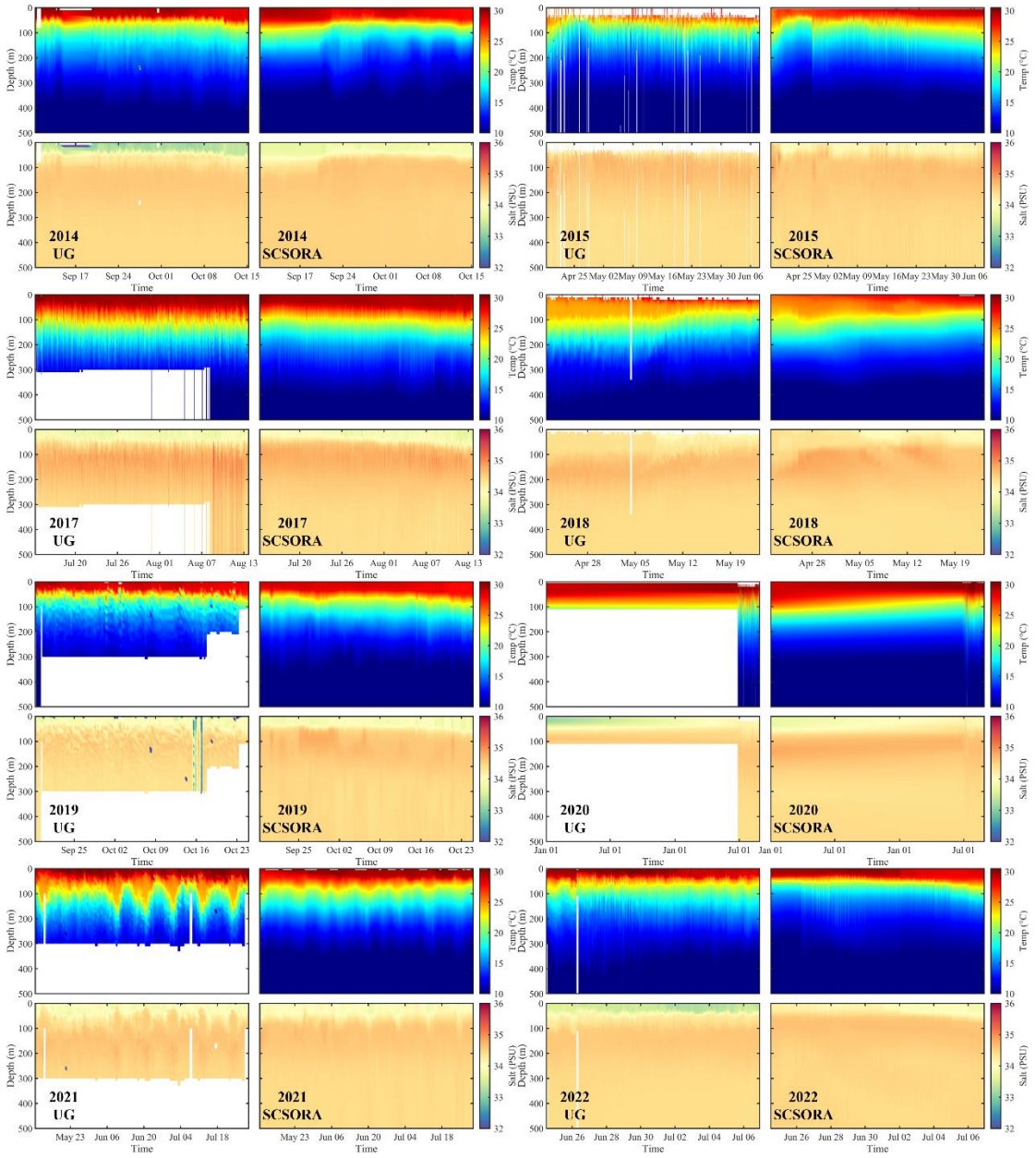


Figure 8. Comparison of vertical section time series of temperature (upper panels) and salinity (lower panels) between UG observations (left column) and SCSORA simulations (right column) from 2014 to 2022."

(2) We have added MLD validation based on glider observations in Section 3.3 (Lines 527-535) as Figure 10. The figure caption reads:

" In addition, the annual mean bias between the MLD derived from UG and that from SCSORA was calculated (Figure 10) to evaluate the capability of SCSORA in reconstructing the upper-ocean vertical mixing structure in the northern SCS. The results show that, except for 2014 when the bias is close to 0 m, the MLD simulated by SCSORA is generally deeper than that observed by the UG. Among these, the biases in 2017, 2018, and 2022 are the most pronounced, with mean biases of approximately −6.4, −6.1, and −6.9 m, respectively; the biases

during 2019–2021 are relatively smaller, ranging from approximately −3.6 to −4.4 m. The interannual variability of the median bias is highly consistent with that of the mean bias.

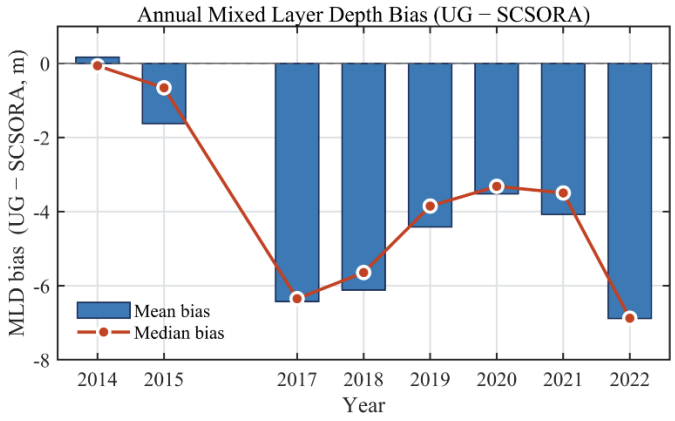


Figure 10. Annual mean and median MLD bias between the UG observations and SCSORA (UG − SCSORA) from 2014 to 2022. Blue bars denote the annual mean bias, and the red line with dots denotes the annual median bias."

7. Validation of high-wavenumber variability

- The spectral analysis (Fig.7 & 8) shows that SCSORA contains substantially more energy at high wavenumbers than the coarser reanalysis and observation products. However, the presence of high-wavenumber energy alone does not necessarily show that these small-scale signals are realistically reproduced. The authors are encouraged to provide further validation against available high-resolution observations, where feasible (e.g., SWOT), or otherwise discuss the effective spatial resolution and limitations of interpreting the high-wavenumber spectral energy.

Response: We first attempted to use high-resolution SWOT along-track SLA data to independently validate the high-wavenumber variability of SCSORA. The data used are the Copernicus Global Ocean Along-Track L3 Near-Real-Time Sea Surface Height product (https://doi.org/10.48670/moi-00147). The results show that during the verifiable period (July–December 2024), the mean RMSE between SCSORA and SWOT along-track SLA is approximately 8.9 cm (Figure R2). However, this SWOT dataset only covers the period after July 2024, and its limited temporal length is insufficient to comprehensively evaluate the quality of SCSORA's high-wavenumber variability over the entire 24-year record, nor is it sufficient to make a complete judgment on the quality of the results for the full year 2024. Therefore, we further discuss the effective spatial resolution and interpretive limitations of SCSORA's high-wavenumber spectral energy in the revised manuscript (Lines 633-645).

The revised text states that SCSORA exhibits a continuous spectral energy distribution in the submesoscale wavenumber range (10^{-2} to 10^{-1} cpkm), with a spectral slope between k^{-3} and k^{-2}, consistent with the expected spectral characteristics of the transition from mesoscale quasi-geostrophic to submesoscale ageostrophic processes. It should be emphasized, however, that

spectral analysis itself mainly reveals the structural characteristics of energy at different scales, and high-wavenumber energy does not necessarily correspond to real physical processes. The horizontal grid spacing of SCSORA is approximately 1/30°, but the effective resolution of an ocean model is usually determined by the numerical dissipation scale and is influenced by factors such as the density of assimilated observations, the localization scale of the background error covariance, model physical parameterizations, and grid-scale numerical noise; it cannot simply be equated with the grid resolution. Previous studies have shown that model spectra often exhibit "roll-off" and spurious fluctuations at the high-wavenumber end, and these features do not necessarily correspond to real dynamical processes (Paul et al., 2025). Therefore, before using SCSORA for studies of smaller-scale dynamical processes, it is still necessary to evaluate its reliability at these scales in combination with longer time series and higher-resolution observational data.

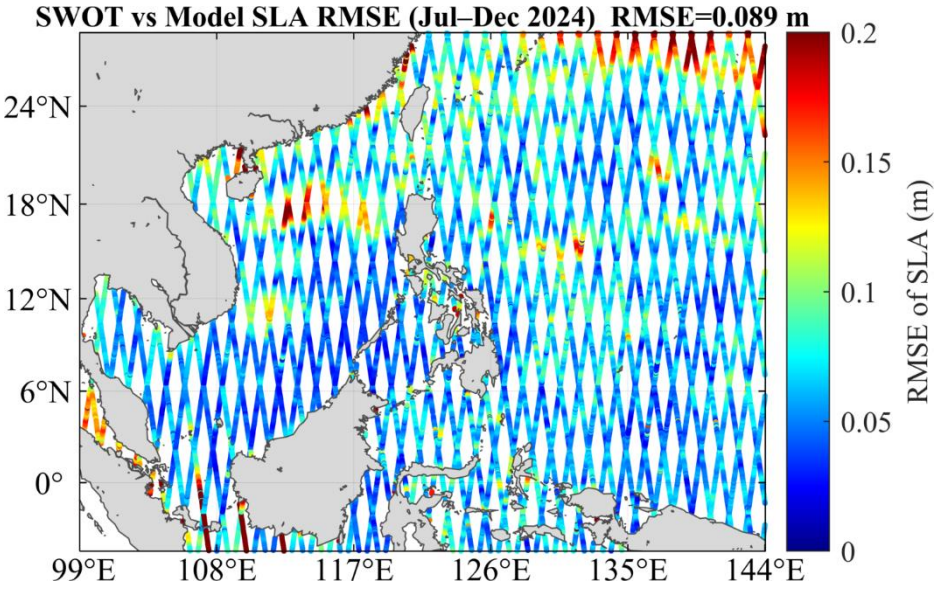


Figure R2. Spatial distribution of SLA RMSE between SWOT and SCSORA (Jul–Dec 2024).

Changes in the manuscript:

We have added a discussion of the effective spatial resolution and the interpretive limitations of the high-wavenumber spectral energy in Section 4.2 (Lines 633-645). The added text reads:

"The above spectral analysis results indicate that SCSORA holds potential for characterizing smaller-scale oceanic variability. However, spectral analysis itself primarily reveals the structural characteristics of energy distribution across different scales. The horizontal grid spacing of SCSORA is approximately 1/30°, yet in ocean models the effective resolution is generally determined by the numerical dissipation range (Soufflet et al., 2016) and is influenced by factors such as the density of assimilated observations, the localization scale of background error covariances, model physical parameterizations, and grid-scale numerical

noise (Li et al., 2024); it therefore cannot be simply equated with the grid resolution. Previous studies have shown that model spectra often exhibit a "roll-off" and spurious fluctuations at high wavenumbers, and these features do not necessarily correspond to real physical processes (Paul et al., 2025). Consequently, before applying SCSORA to the study of smaller-scale dynamical processes, its reliability at these scales should be evaluated against longer time-series of higher-resolution observational data. It should be noted that the present spectral analysis focuses on the scale distribution of energy rather than dynamical energy exchange. After the reliability of SCSORA at smaller scales is further validated, its high-resolution output could be used to diagnose eddy–mean energy exchange through eddy flux ellipse frameworks (Chen et al., 2024)."

8. MHW analysis

- The MHW analysis in Section 4.2 is useful as an application example of SCSORA. However, the differences between SCSORA and OSTIA may partly reflect multiple factors, including the influence of assimilated OISST and the model dynamics. Therefore, statements suggesting superior temporal continuity or event stability of SCSORA (ex. L401) should be interpreted more cautiously, as these differences do not necessarily indicate better representation of MHWs. Without additional independent observations, it is difficult to determine which representation is more realistic.

Response: In the revised manuscript, statements in the original manuscript regarding the superior temporal continuity or event stability of SCSORA (around line 401 of the original manuscript) have been deleted. The revised Section 4.2 (Lines 716-735) no longer makes judgments about the relative merits of the MHW representations of SCSORA and OSTIA, but instead focuses on the consistency and differences in their spatial distributions and interannual variability.

The revised results show that during 2001–2024, the spatial distributions of MHWs in SCSORA and OSTIA are generally consistent, both exhibiting pronounced spatial inhomogeneity: MHW frequency in the northern SCS is markedly higher than that in the south, and the maximum intensity also shows a north-high, south-low distribution, with the Taiwan Strait being the region with the strongest MHW intensity in both products. In the two subregions, NSCS and NWPO, SCSORA, OSTIA, and OISST are generally consistent in the interannual variability of MHW frequency, duration, and cumulative intensity, all showing increasing trends that are particularly pronounced after 2010. In 2024, the cumulative intensity recorded by SCSORA exceeds 25°C·days, the highest value over the entire record; OISST shows a similar high value, whereas the OSTIA peak is relatively lower. Further comparisons based on daily-scale SST, climatology, and MHW thresholds in the NSCS and NWPO for 2024 (Figure. 16) show that the three products generally exhibit a consistent seasonal cycle, with SST reaching its minimum in January–March and its peak in June–September, and the threshold curve lying clearly above the climatology. However, differences exist at the event scale: the

events identified by SCSORA have longer durations (up to 34 days) and slightly lower peak intensities (0.71°C); the events identified by OSTIA have the second-longest durations (up to 23 days) and slightly higher peak intensities (0.75°C).

Changes in the manuscript:

(1) We have removed the statements implying that SCSORA is superior in terms of temporal continuity or event stability, and revised Section 4.2 (Lines 716–735) to focus on the consistency and differences among SCSORA, OSTIA, and OISST in the spatial distribution and interannual variability of MHWs. The revised text now reads:

" Figure 16 presents the daily SST, climatology, and MHW thresholds based on SCSORA, OSTIA, and OISST for the NSCS and NWPO subregions in 2024, with MHW events exceeding the threshold marked by red shading. Overall, the three products exhibit a consistent seasonal cycle: SST reaches its minimum value during January–March and its peak value during June–September, while the threshold curve lies distinctly above the climatology, defining the identification criterion for MHWs (Hobday et al., 2016). In the NSCS, all three products identify significant summer MHW events, but differences exist at the event scale. The SCSORA SST time series is relatively smooth with weaker high-frequency fluctuations, resulting in longer event durations (up to 34 days) and slightly lower peak intensities (0.71°C). OSTIA is more sensitive to high-frequency variability, capable of capturing shorter events (up to 23 days), with slightly higher peak intensities (0.75°C). In the NWPO, the MHW signal is generally weaker, with lower duration and intensity; the strongest events recorded by the three products differ, with SCSORA at 0.64°C, OSTIA at 0.46°C, and OISST at 0.53°C. OISST exhibits a variation trend broadly consistent with SCSORA, but with MHW intensity and MHW duration slightly lower than those of SCSORA."

(2) We have added the OISST-based MHW distribution to Figure 16.

"

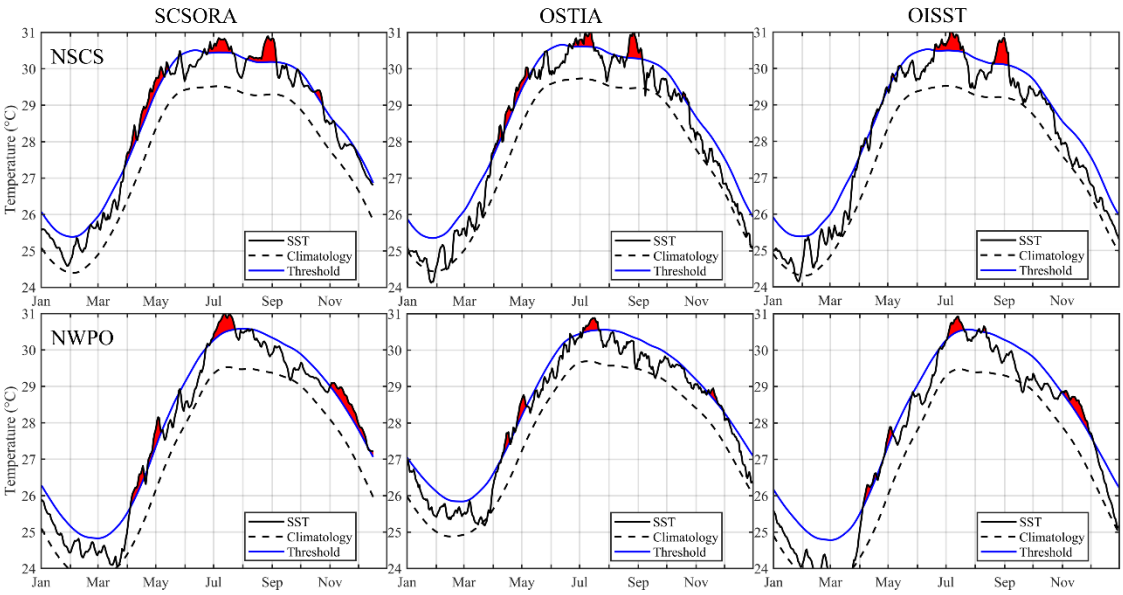


Figure 16. Seasonal evolution of domain-averaged SST from SCSORA (left column), OSTIA (middle column), and OISST (right column) in the NSCS (top row) and the NWPO (bottom row) for the year 2024. Black solid lines indicate daily mean SST in 2024, black dashed lines indicate climatological mean SST, and blue solid lines indicate the MHW threshold (90th percentile of climatology). Red shading denotes marine heatwave (MHW) events where daily SST exceeds the threshold. "

9. Scientific applications

- Section 4.3 goes considerably beyond demonstrating the potential applications of SCSORA and attempts to provide detailed interpretations of eddy dynamics and their modulation of MHWs. However, some of these process-oriented interpretations are not sufficiently supported by the analyses presented. Given that this is primarily a data paper, I suggest reducing the scope and level of interpretation in Section 4.3 and placing greater emphasis on the validation and characterization of SCSORA in Section 3. Section 4.3 could instead be more concisely presented as an example demonstrating the potential utility of the 3-D reanalysis for studying mesoscale eddies and their relationship with MHWs.

Response: Section 4.3 of the revised manuscript (Lines 742-927) has been trimmed and modified. The revised section, on the one hand, focuses on the eddy count statistics and their comparison with AVISO (Figure. 17). On the other hand, using three representative eddies as examples to demonstrate the ability of SCSORA to resolve the three-dimensional structure of MHWs in eddy regions (Figure. 18). Regarding the eddy statistics, we present the number, interannual variability, and seasonal variation characteristics of cyclonic and anticyclonic eddies in the eddy-active region of the SCS (102–122°E, 5–24°N) based on SCSORA and AVISO (Figure. 17). The results show that SCSORA and AVISO are generally consistent in interannual variability, but SCSORA identifies slightly more eddies, especially during 2022–

2024; both show an increasing trend during 2020–2023, with the increase in SCSORA being more pronounced.

Regarding the three-dimensional structure of MHWs, in the anticyclonic eddy case, the positive MHW anomaly can extend below 200 m; in the cyclonic eddy case, the positive anomaly is weaker at the eddy center and forms an arc-like or ring-like pattern at the edges, producing a "weak center, strong edge" structure; in the double anticyclonic eddy case, both eddies show positive surface anomalies, but their subsurface structures differ, with one exhibiting a subsurface-intensified MHW and the other exhibiting a subsurface reverse cooling anomaly. The above examples demonstrate the potential utility of SCSORA for studying mesoscale eddies and their relationship with MHWs, and can provide a data basis for related analyses.

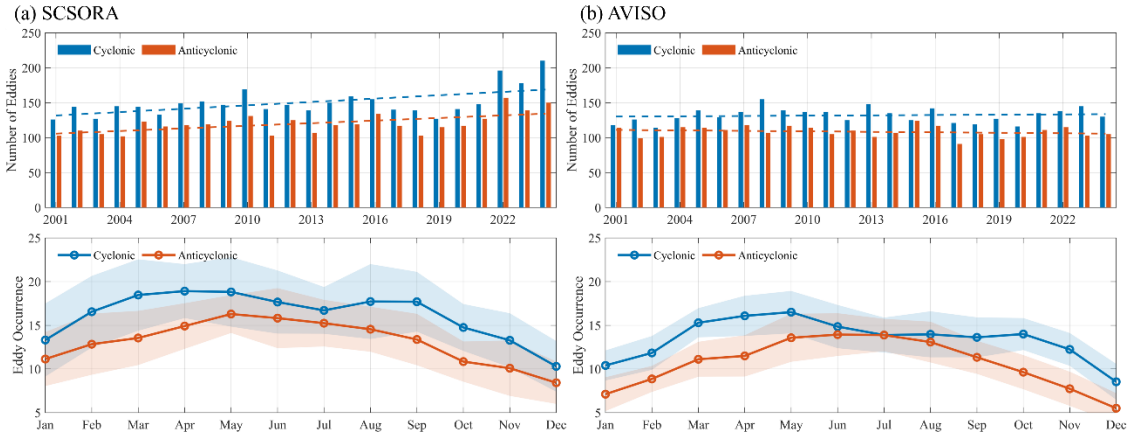


Figure 17. Statistical characteristics of cyclonic (blue) and anticyclonic (orange) eddies in the SCS identified from SCSORA (left column) and AVISO (right column). Top row shows the interannual variation in eddy numbers during 2001–2024, with dashed lines indicating the corresponding linear trends. Bottom row shows the monthly climatological eddy occurrence, with solid lines representing multi-year monthly means and shading indicating the interannual variability range for each month.

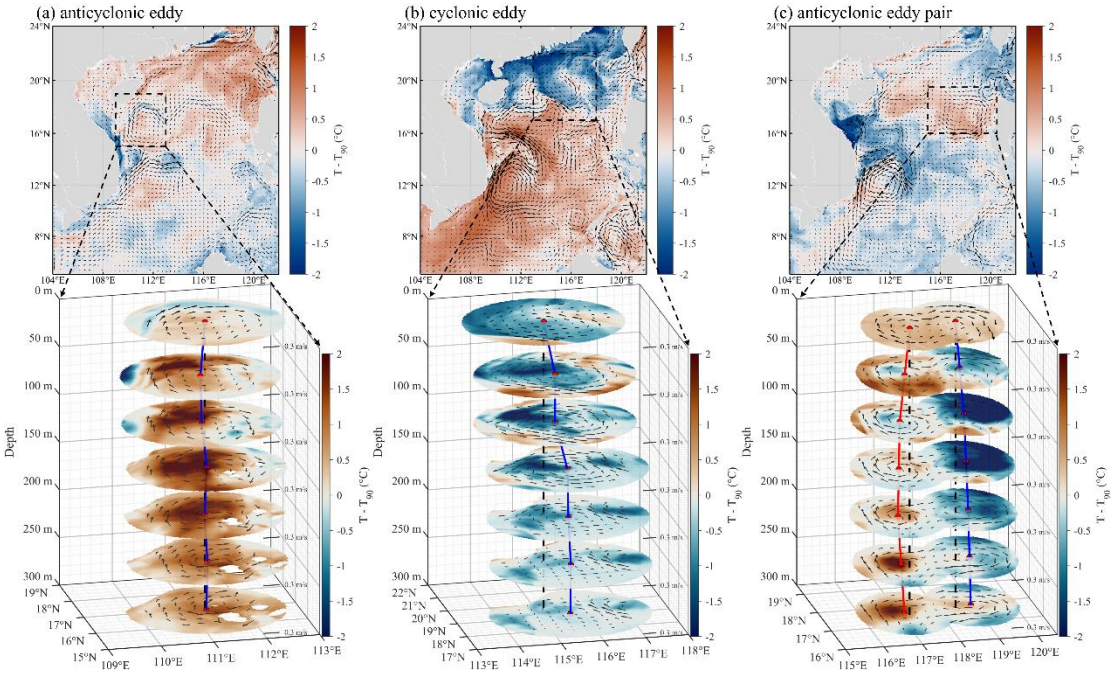


Figure 18. 3D structure of MHWs in representative eddy-controlled regions. Left, middle, and right columns correspond to an anticyclonic eddy, a cyclonic eddy, and a compound double-anticyclonic eddy structure, respectively. Top row shows the SST anomaly ($T-T_{90}$, units: °C) with black arrows indicating surface currents and black dashed boxes marking the eddy-influenced region. Bottom row shows the 3D vertical structure of MHW temperature anomalies ($T-T_{90}$) within the corresponding eddy region (depth range: 0–300 m), with black arrows on each horizontal slice indicating the current field at that depth level, and vertical colored lines marking the eddy center positions and their lateral displacement with depth.

Changes in the manuscript:

We have removed Figure 13 and its related content from the original manuscript and rewritten Section 4.3 (Lines 742-927) to reduce the scope and level of interpretation, focusing instead on eddy count statistics and their comparison with AVISO (Figure 17), and on using three representative eddies as examples to demonstrate the ability of SCSORA to resolve the three-dimensional structure of MHWs in eddy regions (Figure 18), thereby presenting the section more concisely as an application example. The revised text now reads:

" The statistical results indicate that in the eddy-active region of the SCS (102–122°E, 5–24°N), cyclonic eddies outnumber anticyclonic eddies (Figure. 17). SCSORA and AVISO are generally consistent in interannual variability, but SCSORA identifies a slightly higher number of eddies, especially during 2022–2024. Notably, both AVISO and SCSORA exhibit an increasing trend during 2020–2023, with a more pronounced increase in SCSORA, especially during 2022–2024. Eddy activity in the SCS is modulated by the monsoon, ENSO, and PDO through local wind stress curl (Wang et al., 2003; Cheng and Qi, 2010; He et al., 2016). The

negative PDO and consecutive La Niña conditions in the 2020s may favor cyclonic eddy generation; meanwhile, the Kuroshio intrusion through the Luzon Strait can enhance frontal and shear instability in the NSCS, also favoring the generation of new eddies (Wu and Chiang, 2007). In addition, differences in effective resolution among datasets may also affect the comparison of eddy counts. Such method- and resolution-dependent discrepancies are common in eddy detection and eddy data products (Dong et al., 2025). However, the specific mechanisms can only be clarified through dedicated sensitivity experiments and validation against higher-resolution observations. In terms of seasonal variability (bottom row of Figure. 17), cyclonic eddies exhibit a bimodal distribution, with two peaks occurring in March–May and August–October, respectively. In contrast, the seasonal variability of anticyclonic eddies is weaker, manifesting only as a single broad peak in May–August.

While most MHW studies based on the 90th percentile threshold have focused on the 2D distribution of SST anomalies (He et al., 2024; Oliver et al., 2021; Sun et al., 2026; Wyatt et al., 2023; Yao et al., 2024), the limited availability of 3D temperature data has hindered analysis of their subsurface structure. Mesoscale eddies themselves possess complex three-dimensional structures, including vertical tilt and subsurface coherence (Zhang et al., 2024), which may further modulate the subsurface structure of MHWs. Using SCSORA, we present illustrative examples of the three-dimensional (3D) structure of MHWs under three representative eddy configurations: an anticyclonic eddy, a cyclonic eddy, and a double-anticyclonic eddy pair (Figure 18). The analysis covers the upper 300 m, with temperature anomalies defined as $T - T_{90}$ and surface and subsurface currents shown as vectors.

In the anticyclonic eddy case (Figure 18a), positive MHW temperature anomalies appear at all depth levels, with values exceeding 1.5°C near the surface and remaining positive below 200 m, indicating that the MHW signal extends well into the subsurface. In the cyclonic eddy case (Figure 18b), positive anomalies are weak at the eddy center but form arc- or ring-shaped patterns at the eddy periphery, with anomalies reaching approximately 1°C. This produces a center-weak, edge-strong structure that is not evident from SST alone. In the double-anticyclonic eddy case (Figure 18c), both eddies show positive surface anomalies, but their subsurface structures differ: one exhibits a subsurface-enhanced MHW with positive anomalies extending below 200 m, while the other displays a subsurface-reversed (cooling) anomaly, with negative values emerging below the surface layer. The colored vertical lines in Figure 18 further indicate that the eddy centers are not perfectly vertical but shift laterally with depth, suggesting that the 3D structure of MHWs is closely tied to the vertical coherence of the eddy field.

These examples demonstrate that SCSORA can resolve the 3D structure of MHWs under different eddy configurations and can serve as a useful data basis for investigating eddy–MHW interactions. A comprehensive dynamical interpretation, however, is beyond the scope of this data-oriented paper and requires further analysis with independent observations."